Research Article

Azzh Saad Alshehry, Saima Noor*, Syed Arshad Abas, Mehreen Fiza, and Hakeem Ullah*

Analysis of MHD hybrid nanofluid flow over cone and wedge with exponential and thermal heat source and activation energy

https://doi.org/10.1515/phys-2025-0194
received January 11, 2025; accepted May 07, 2025

Abstract: Hybrid nanofluids, an advanced class of working fluids, gained significant attention due to their superior thermal performance and heat transfer characteristics. These fluids consist of two types of nanoparticles suspended in a base fluid, offering enhanced thermal performance, making them crucial in engineering applications. In many industrial processes, magnetohydrodynamic (MHD) hybrid nanofluid flow plays a vital role in controlling mass and heat transfer in systems involving precipitation and chemical processing. The interaction between thermal radiation, chemical reactions, Joule heating, and heat sources significantly affects the efficiency of such systems, necessitating an in-depth analysis of their combined effects. This study focuses on the heat and mass transfer in hybrid nanofluid flow over various geometries, which is crucial for thermal management in electronic devices, precipitation, and filtration processes. Practical applications of a hybrid nanofluid flow around cones and wedges include spacecraft design, nuclear reactors, solar power collectors, *etc.* Therefore, this research examines the MHD hybrid nanofluid flow over a cone and wedge, using a suspension of SWCNTs and MWCNTs as nanomaterials in H_2O as the base fluid. The study also considers the impact of Joule heating, an exponential space-based heat source in the temperature equation with thermal and mass convective conditions over two geometries (cone and wedge). Additionally, chemical reactions play a significant role in various natural and industrial processes. With this initiation, this research explores the effect of the activation energy and binary chemical reaction on the MHD hybrid nanofluid flow. The hybrid nanofluid model over two different geometries is governed by partial differential equations and converted to ordinary differential equations using similarity variables. The bvp4c method in MATLAB was employed to solve these equations numerically. The effects of the sundry flow parameter on the velocity, temperature, and concentration distributions were determined and discussed briefly. The study's findings show that the improvement in both the thermal and mass Grashof numbers results in an increase in the velocity profile, supporting the effectiveness of hybrid nanofluids in cooling technologies for electronic devices. The increasing impression of the activation energy and mass Biot number on the concentration profile is progressive for wedges compared to cones. Furthermore, the results reveal that the presence of a nonlinear heat source tends to intensify the thermal profiles for wedges more significantly than the flow over cones, which is also related to the application of solar power collectors. The rate of heat transfer for the flow over a cone case is higher for the growing estimation of radiation, and the Biot number is particularly relevant to high-temperature applications such as nuclear reactors and spacecraft. The increasing impact of the Schmidt number, chemical reaction, and mass Biot number on the mass transfer rate is higher for cones as compared to wedges, while the activation energy has an opposite behavior for both flow cases. The observed trends in the mass transfer rate also support filtration and separation technologies, optimizing their efficiency based on fluid and material properties.

Keywords: hybrid nanofluid, Joule heating, convective and mass flux boundary conditions, exponential heat source, bvp4c

*** Corresponding author: Saima Noor**, Department of Basic Sciences, General Administration of Preparatory Year, King Faisal University, P.O. Box 400, 31982, Al Ahsa, Saudi Arabia; Department of Mathematics and Statistics, College of Science, King Faisal University, P.O. Box 400, 31982, Al Ahsa, Saudi Arabia, e-mail: snoor@kfu.edu.sa
*** Corresponding author: Hakeem Ullah**, Department of Mathematics, Abdul Wali Khan University Mardan, 23200, Khyber Pakhtunkhwa, Pakistan, e-mail: hakeemullah1@gmail.com
Azzh Saad Alshehry: Department of Mathematical Sciences, Faculty of Sciences, Princess Nourah bint Abdulrahman University, PO Box 84428, Riyadh, 11671, Saudi Arabia
Syed Arshad Abas: Department of Mathematics, Abdul Wali Khan University Mardan, 23200, Khyber Pakhtunkhwa, Pakistan, e-mail: abbasarshad47@gmail.com
Mehreen Fiza: Department of Mathematics, Abdul Wali Khan University Mardan, 23200, Khyber Pakhtunkhwa, Pakistan

Open Access. © 2025 the author(s), published by De Gruyter. This work is licensed under the Creative Commons Attribution 4.0 International License.

Nomenclature

E	activation energy
β	acute angle
T_∞	ambient temperature
α	angle of inclination
Nb	Brownian motion
x, y	Cartesian coordinates
Kr	chemical reaction
C	concentration
ρ	density
μ	dynamic viscosity
Ec	Eckert number
σ	electrical conductivity
q_w	heat flux
h_f	heat transfer coefficient
υ	kinematic viscosity
L	length
M	magnetic field
q_m	mass flux
Gc	mass Grashof number
h_m	mass transfer coefficient
k_r	mean absorption coefficient
$\varphi_{1,2}$	nanoparticle volume fraction
Nu_x	Nusselt number
Pr	Prandtl number
Ω	rate of chemical reaction
R_d	Reynolds number
Sc	Schmidt number
τ_w	shear stress
Sh_x	Sherwood number
ξ	similarity variable
C_{fx}	skin friction
α	solutal Biot number
$\widehat{\beta_C}$	solutal expansion coefficient
Qe	space-based heat source
$\widehat{C_\mathrm{p}}$	specific heat
B_0	strength of the magnetic field
u_w	stretching velocity
T	temperature
δ	temperature difference parameter
γ	thermal Biot number
k	thermal conductivity
$\widehat{\beta_T}$	thermal expansion coefficient
Gr	thermal Grashof number
Q_1	thermal heat source
Rd	thermal radiation
u, v	velocity components

1 Introduction

The main hindrances of base liquids are their low thermal conductivity and moderate heat transfer capability, which prevent them from meeting the requirements of emerging engineering and technology sectors. Choi and Eastman [1] offered an excellent answer to this problem by coining the term nanofluid. The addition of a diverse range of nano-sized materials can significantly improve the efficiency of the base liquid. This is because nanomaterials possess enhanced thermal, physical, and chemical properties, greatly enhancing the thermal transfer performance. Research on the thermal transport of nanoliquid flows has been significantly enhanced in the past decade owing to the widespread choice of applications in current technology, such as electronic and motor cooling, nuclear reactors, medical science, and the textile industry. The exponential extending surface nanofluid model has significant applications in industrial processes, such as energy systems, medical devices, and electronic cooling, where controlling the heat transfer is essential for efficiency [2,3]. Das [4] analyzed the slip condition to investigate the nanofluid flow over a nonlinear elongating surface. The effect of combined nanoparticles on mixed convective magnetohydrodynamic (MHD) stagnation point flow was investigated by Mahmood *et al.* [5] using the Krieger–Dougherty and Maxwell–Bruggeman models. Compared to the homogeneous model, the aggregation model has a higher viscosity, which leads to an increase in the velocity profile. The chemically reacted MHD Maxwell nanofluid flow across an extended rotating porous cylinder was inspected by Khan *et al.* [6]. They observed that the velocity panel increased with the buoyancy factor and decreased with the porosity and bio-convection factors. Poply [7] used the Buongiorno model to study the heat transfer properties of a boundary-layer MHD nanofluid flow over an extended surface. Ramzan et al. [8] explored the thermal slip flow of ethylene glycol-based MHD nanofluids over an exponentially stretched surface. They found that in both prescribed exponential surface temperature and heat flux conditions, the temperature of the fluid increases with radiation.

There has been a significant increase in studies focusing on hybrid nanofluids. The term hybrid nanofluid refers to a more advanced type of nanofluid that is composed of two dissimilar nanoparticles combined with a base fluid. As a result of their thermal qualities, hybrid nanofluids have emerged as a new dawn for young researchers and academics. Kumar [9] studied a convective

hybrid nanofluid containing copper and ferrous oxide nanoparticles. They found that the rate of heat transfer was enhanced for the nanofluid compared with the hybrid. Arif *et al.* [10] studied the heat transfer improvement of engine oil-based hybrid nanoliquid with activation energy. The concentration profile was enriched with an increasing activation factor. Galal *et al.* [11] examined the non-equilibrium effects for ternary hybrid nanofluid flow over a two-dimensional stretching surface with an exponential heat source. Abas *et al.* [12] used a non-Newtonian model to study a hybrid nanofluid flow with copper and alumina nanoparticles. Vishalakshi *et al.* [13] examined the heat transfer characteristics of mixed convicted incompressible hybrid nanofluid MHD flow with thermal radiation. They concluded that the tangential velocity improved in both the suction and injection cases with a higher Rayleigh number. The thermal profile of the hybrid nanofluid is higher for a hybrid nanofluid flow over a stretching surface under convection and zero mass flux conditions [14]. Abbas *et al.* [15] numerically examined the hybrid nanofluid over a nonlinear exponential porous curved surface. The velocity profile escalated with the nanoparticle concentration in the presence of suction and injection. Lone *et al.* [16] analyzed the MHD micropolar hybrid nanofluid containing silver and alumina nanoparticles flow across a plate. They deduced that the radiation factor increased the Nusselt number. Kolsi *et al.* [17] highlighted that the heat source significantly affected the thermal profile of the hybrid nanofluid. The hybrid nanofluid enhances the Nusselt number owing to its greater thermal conductivity, as revealed by Ahmad *et al.* [18]. Murtaza *et al.* [19] examined numerically the heat transport characteristics of hybrid nanofluid flow in a channel and found that the rate of heat transfer improved 12.01% for ternary hybrid nanofluid. Zangooee *et al.* [20] reported the slip effects on hybrid nanoliquid flow over a vertical plate in the attendance of suction. They found that the higher the velocity slip factor, the higher the heat transfer, which increased to 5.63%. The thermal profile is enhanced by nanoparticle interactions [21]. A higher heat source parameter increases the heat transfer rate, while the slip parameter impacts the fluid motion. These hybrid nanofluids are promising for use in energy systems and high-performance heat exchangers. To analyze two viscosity models over disks under various conditions [22], such as thermal and exponential heat sources with chemical reactions, to better understand their applications in industrial and biomedical science. Galal *et al.* [23] used the Hamilton–Crosser thermal conductivity and Xue models to examine the effects of thermal radiation and exponential heat source on hybrid nanofluid flow under slip conditions.

Scientists have recently gained interest in studying the boundary layer fluid flow performance over different geometries (cones, wedges, and plates). This research has practical applications in various fields, including engineering, industry, solar collectors, cooling systems, heat exchangers, geosciences, aeronautical processes, and astrophysics. The convective flow over a cone and wedge was investigated by Dawar *et al.* [24] using the hopmotopic solution for the Williamson nanofluid. When compared to the wedge, it has been discovered that the cone has a stronger impact on the growth velocity of Newtonian and Williamson nanofluids. Paul *et al.* [25] examined the slip effect on the Casson hybrid nanofluid unsteady flow over a rotating cone. Their findings revealed that skin friction was boosted by 52% in the case of the Casson hybrid nanofluid. By studying the temperature-dependent fluid property, John *et al.* [26] observed the three-dimensional flow of H_2O-based hybrid nanoliquid in a static cone-disk system. They noted that improving the addition of nanometer-sized particles improves the heat transfer. Peter *et al.* [27] inspected numerically the efficiency of heat and mass transfer on non-Newtonian MHDs hybrid nanofluid flow over a cone or plate surface. They noted that both magnetic and thermal radiation improved the heat and mass rate. Using a stationary permeable cone, Yahaya *et al.* [28] explored the mixed convection flow of a hybrid nanofluid. The velocity curves of the hybrid nanoliquids were enhanced with a higher mixed convection factor, but the temperature profile was reduced. Using the Chataneo-Christov model and thermal radiation, Dawar *et al.* [29] studied the heat transmission of a hybrid nanoliquid flow across cone/wedge/plate geometries. They discovered that equating to the base fluid, the effects of the magnetic factor and thermal Grashof number are 38% and 47% larger, respectively, for hybrid nanofluid flow.

Both single-wall (SWCNTs) and multi-wall carbon nanotubes (MWCNTs) are allotropes of carbon that have a wide range of practical uses. Some examples of these applications include optics, batteries, microelectronics cooling, water purification, drug delivery, ultra-capacitors, and a variety of industries. Iijima [30] was the first to establish the concept of carbon nanotubes. He also distinguished between two different forms of carbon nanotubes, SWCNT and MWCNT. Akbar *et al.* [31] explored the heat transfer properties of hybrid nanofluid containing MWCNT and SWCNT nanoparticles over a heated extended surface. They explored the numerical method bvp4c for the simulation and found that the heat-transport rate improved in the Xue model. A comparative study of hybrid and nanofluids was conducted by Haider *et al.* [32] across an extended surface. According to their findings, the temperature profile was enhanced more with the (SWCNT-MWCNT/water) than with SWCNT/water. Kumar [33] investigated the boundary layer flow of a hybrid nanofluid based on carbon nanotubes across a moving surface with an exponential velocity. The three-dimensional flow of a hybrid nanofluid containing carbon nanotubes over a heated surface was

numerically investigated by Nadeem *et al.* [34]. They noted that the surface drag and rate of heat transmission were both improved by the hybrid nanofluid, which consisted of single- and multi-walled carbon nanotubes. The heat transfer feature of an SWCNT-MWCNT/propylene glycol hybrid nanofluid flowing across a porous expanding surface was inspected by Gupta *et al.* [35]. They found that the Eckert and Biot numbers both had opposite impacts on the temperature trace.

Another interesting factor for application to boundary layer flow problems is Joule heating or Ohmic heating, which has a large impact on the flow of MHD fluids. Applying Joule heating to electrical energy reduces the resistance in the material, which in turn produces thermal energy. Asghar *et al.* [36] conducted research on the characteristics of MHDs in a hybrid nanofluid containing copper and alumina particles suspended in water over an extending/shrinking surface. Their study considered both Joule heating and thermal radiation. According to their research, the Eckert number and radiation parameter values were directly proportional to the temperature profiles of the dual solutions. EI-dawy *et al.* [37] reported a numerical investigation of both Joule heating and viscous dissipation on hybrid micropolar flow in the light of thermal radiation. According to their findings, temperature curves are amplified with magnetic and heat source factors. Abbas *et al.* [38] studied the Cattaneo–Christov heat flux model regarding hybrid nanofluid flow over a disk with Joule heating effects. Khan *et al.* [39] scrutinized the effects of heat creation and absorption, as well as Joule heating, which is responsible for controlling the generation of entropy and the transit of heat in Darcy–Forchheimer flow, which is passed over a stretched nonlinear surface. The temperature and entropy rate were both improved for the radiation variable. Ullah *et al.* [40] studied the ternary hybrid nanofluid with joule heating and found that the thermal profile improved with higher Eckert number. Sulochana and Shivapuji [41] considered the MHD flow of a hybrid nanofluid with Joule heating and viscous dissipation past an extending surface. The influence of the magnetic field and Joule heating along a convective stretching/shrinking sheet was investigated by Zhang *et al.* [42]. The stagnation point flow, including Joule heating and viscous dissipation, was investigated by Rafique *et al.* [43] using a hybrid model. They found that increasing the magnetic parameters improved the skin friction coefficient.

Based on the motivation from the above-cited literature, this study extends the existing model [44] by analyzing the flow of a hybrid nanofluid containing SWCNT and MWCNT nanoparticles over two different geometries (cones and wedges). The effects of the magnetic field, thermal radiation, and first-order chemical reaction have been explored in previous studies over two different geometries. The goal of the present work is to examine the physical significance of MHD, Joule heating, and the combined effect of linear and exponential space-based heat sources over an incompressible hybrid nanofluid across a cone and wedge. Furthermore, the Arrhenius activation energy along the binary chemical reaction factors is incorporated in the mass equation, whereas at the boundary, the thermal and mass convective conditions are considered in the model. The governing flow problem is framed in the form of a coupled system of non-linear partial differential equations, which are transformed into non-dimensional ordinary differential equations (ODEs). The system of equations is solved numerically using the bvp4c package in the MATLAB environment. The impact of different physical factors is plotted to better understand the flow model. This study aims to answer the following research questions:

1) How does the combined effect of linear and exponential space-based heat sources influence the thermal distribution over cone and wedge geometries?
2) How does the inclusion of the Arrhenius activation energy and binary chemical reactions affect the concentration profile and mass transfer rate?
3) What are the comparative differences in the flow nature and heat and mass transfer between the cone and wedge geometries under the given physical conditions?
4) What role do MHD, Joule heating, and thermal and mass convective boundary conditions play in flow behavior?

For the solution of the modeled problems, the analytical and numerical methods are used. The analytical technique necessitated the appropriate choice of the initial estimate, which is sensitive to the assumption of small parameters [45–48]. An inappropriate choice of assumptions might impact the findings. Numerical techniques [49–52] are employed to solve nonlinear boundary value problems (BVPs) in order to address these issues. Linearization and discretization [53–55] are necessary for numerical approaches. Small parameter assumptions and first estimate selection are not necessary for these approaches [56,57].

The article is structured as follows: Section 1 provides a literature survey. Section 2 presents the flow model and mathematical statement of the present model. Section 3 introduces the physical quantities of interest. A numerical solution of the proposed problem is determined by utilizing the bvp4c method in MATLAB, and is presented in Section 4. Model validation against previous studies is presented in Section 5. Results and discussion are presented in Section 6. Finally, Section 7 presents the final outcomes and future research directions.

2 Flow model and mathematical statement

In the present problem, consider an incompressible, steady hybrid nanofluid two-dimensional MHD flow over two distinct geometries. Let us assume that u and v are the velocity components along x- and y-axis. The stretching velocity of the surfaces is $u_w = \frac{\upsilon_f x}{l^2}$, where L is the characteristic length. Further, assume that β is the half angle of the cone/wedge with radius r_a and Ω is the full angle of the wedge. A transverse magnetic field of strength B_0^2 is applied along the y-direction. For a convectively heated surface, it is assumed that $T_f > T_w > T_\infty$, where T_f is the reference temperature and T_w is the surface temperature, and T_∞ is the far-field temperature. The concentrations at the surface and ambient are C_w and C_∞, respectively. Figure 1(a) shows a flow sketch of the physical model. Additionally, the given supposition has been made as follows:

(1) The flow is affected by the magnetic field, joule heating, and exponential-based heat source.
(2) The surface is assumed to be convective.
(3) SWCNT and MWCNT are combined with water to form a hybrid nanofluid.
(4) The combined effects of the thermal and mass convective conditions are considered at the boundary.

From the stated assumptions the governing flow equations are as follows [44]:

$$\frac{\partial(r_a u)}{\partial x} + \frac{\partial(r_a v)}{\partial y} = 0, \tag{1}$$

$$\rho_{\text{hnf}}\left(v\frac{\partial u}{\partial y} + u\frac{\partial u}{\partial x}\right) = \mu_{\text{hnf}}\frac{\partial^2 u}{\partial y^2} + g\{(\rho\widehat{\beta})_{\text{hnf}}(T_{\text{f}} - T_\infty) + \widehat{\beta_c}(C_{\text{f}} - C_\infty)\}\text{Cos}(\beta) - \sigma_{\text{hnf}}B_0^2 u, \tag{2}$$

$$\left(u\frac{\partial T}{\partial x} + v\frac{\partial T}{\partial y}\right) = \frac{k_{\text{hnf}}}{(\rho C_{\text{p}})_{\text{hnf}}}\frac{\partial^2 T}{\partial y^2} + \frac{Q_1(T - T_\infty)}{(\rho C_{\text{p}})_{t\text{hnf}}} + \frac{Q_2(T_f - T_\infty)}{(\rho C_{\text{p}})_{t\text{hnf}}}\text{Exp}\left(-m\frac{y}{l}\right) + \frac{\sigma_{\text{hnf}}}{(\rho C_{\text{p}})_{\text{hnf}}}B_0^2 u^2, - \frac{1}{(\rho C_{\text{p}})_{\text{hnf}}}\frac{16\sigma^* T_\infty^3}{3k_f}\frac{\partial^2 T}{\partial y^2}, \tag{3}$$

$$\left(v\frac{\partial C}{\partial x} + v\frac{\partial C}{\partial y}\right) = D_m\frac{\partial^2 C}{\partial y^2} - \Omega\left(\frac{T}{T_\infty}\right)^n (C - C_\infty)\text{Exp}\left(-\frac{E_a}{(k_a T)}\right). \tag{4}$$

In Eqs. (1)–(4), the velocities of the fluid along x- and y- directions are u and v, respectively. Furthermore, μ is the dynamic viscosity, σ is the electrical conductivity, ρ is the density of the fluid, k is the thermal conductivity, C_{p} is heat capacitance, σ^* is the mean absorption coefficient, k_{f} is the Boltzmann constant, hnf is a hybrid nanofluid, and $\widehat{\beta_T}$ and $\widehat{\beta_C}$ are thermal and mass expansion coefficients, respectively.

In the above discussed model, the constraints at the boundary are as follows [24,58]:

$$\begin{cases} \text{At } y = 0: \quad u = u_w = \dfrac{\upsilon_f x}{l^2}, \quad v = 0, \\ \dfrac{k_{\text{hnf}}}{h_{\text{f}}}\dfrac{\partial T}{\partial y} = (T - T_f), \quad \dfrac{D_m}{h_m}\dfrac{\partial C}{\partial y} = (C - C_{\text{f}}), \\ u(y \to \infty) = 0, \quad T(y \to \infty) = T_\infty, \quad C(y \to \infty) = C_\infty. \end{cases} \tag{5}$$

In Eq. (5), the components of the velocity along their respective directions are u and v, the thermal conductivity is k, l is the characteristic length, υ is the kinematic viscosity, T is the temperature, T_f is the reference temperature, C is the concentration, D_{B} is the Brownian diffusion coefficient, and h_f and h_m are the heat and mass transfer coefficients, respectively.

This problem consists of two types of geometries, with the following assumptions:

(a) Cones, for which $d = 1$ and $\beta \neq 0$.
(b) Wedges, for which $d = 0$ and $\beta \neq 0$.

The values of the thermophysical characteristics of the base fluid and CNTs are given in Table 1.

The theoretical models of the nanofluid and hybrid nanofluid are as follows.

In Table 2, φ_1 and φ_2 represent the nanoparticle volume fraction, the subscripts f, nf, hnf are base fluid, nanofluid, and hybrid nanofluids, and 1, 2 are used for the selected nanoparticles.

The set of pertinent similarity transformations are as follows [44]:

$$\begin{cases} \xi = \dfrac{y}{l}, \quad u = \dfrac{\upsilon_{\text{f}} x}{l^2} f'(\xi), \quad v = \dfrac{-\upsilon_{\text{f}}(1+d)}{l} f(\xi) \\ \theta(\xi) = \dfrac{T - T_\infty}{T_{\text{f}} - T_\infty}, \quad \Phi(\xi) = \dfrac{C - C_\infty}{C_{\text{f}} - C_\infty}. \end{cases} \tag{6}$$

Applying Eq. (6) we reduce Eqs. (1)–(4) into the non-dimensional form as follows:

$$\frac{\mu_{\text{hnf}}}{\mu_{\text{f}}} f''' - \frac{\rho_{\text{hnf}}}{\rho_{\text{f}}}(f'^2 - (1+d)ff'') + \frac{(\rho\widehat{\beta})_{\text{hnf}}}{(\rho\widehat{\beta})_{\text{f}}}(\text{Gr}\theta + \text{Gc}\Phi)\text{Cos}(\beta) - \frac{\sigma_{\text{hnf}}}{\sigma_{\text{f}}}Mf' = 0, \tag{7}$$

$$\left(\frac{k_{\text{hnf}}}{k_{\text{f}}} + \frac{4}{3}\text{Rd}\right)\theta'' + \text{Pr}\left\{\frac{(\rho C_{\text{p}})_{\text{hnf}}}{(\rho C_{\text{p}})_{\text{f}}}(1+d)f\theta' + Q_1\theta + \text{Qe}\ \text{Exp}(-m\xi) + \frac{\sigma_{\text{hnf}}}{\sigma_{\text{f}}}\text{MEc}f'^2\right\} = 0, \tag{8}$$

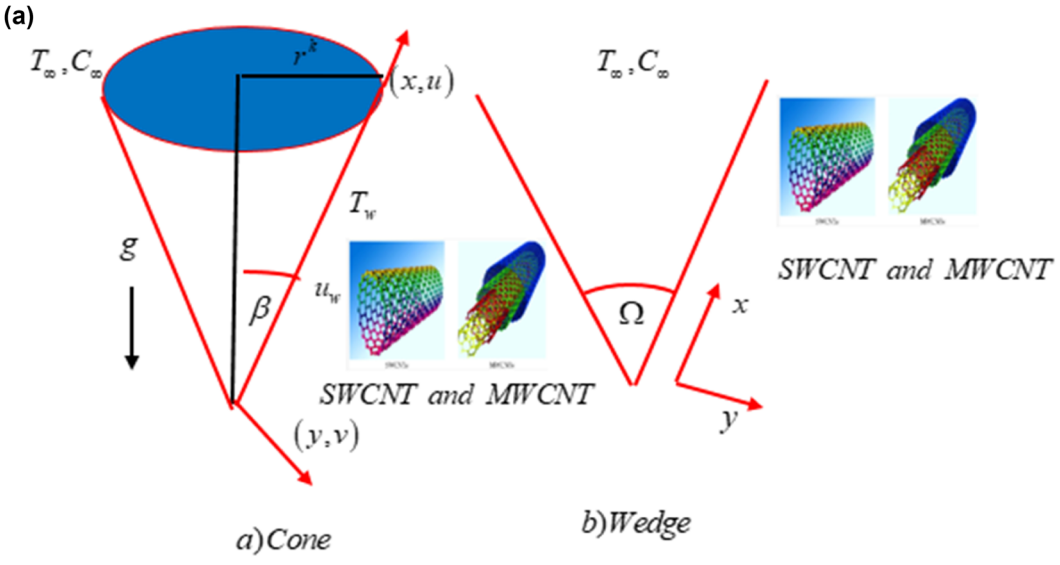

$$\underbrace{v=0\ ,\ -k_{nf}\frac{\partial T}{\partial y}=h_f\left(T_f-T\right),\ -D_m\frac{\partial C}{\partial y}=h_m\left(C_f-C\right)}_{\text{Surface Condiations}}$$

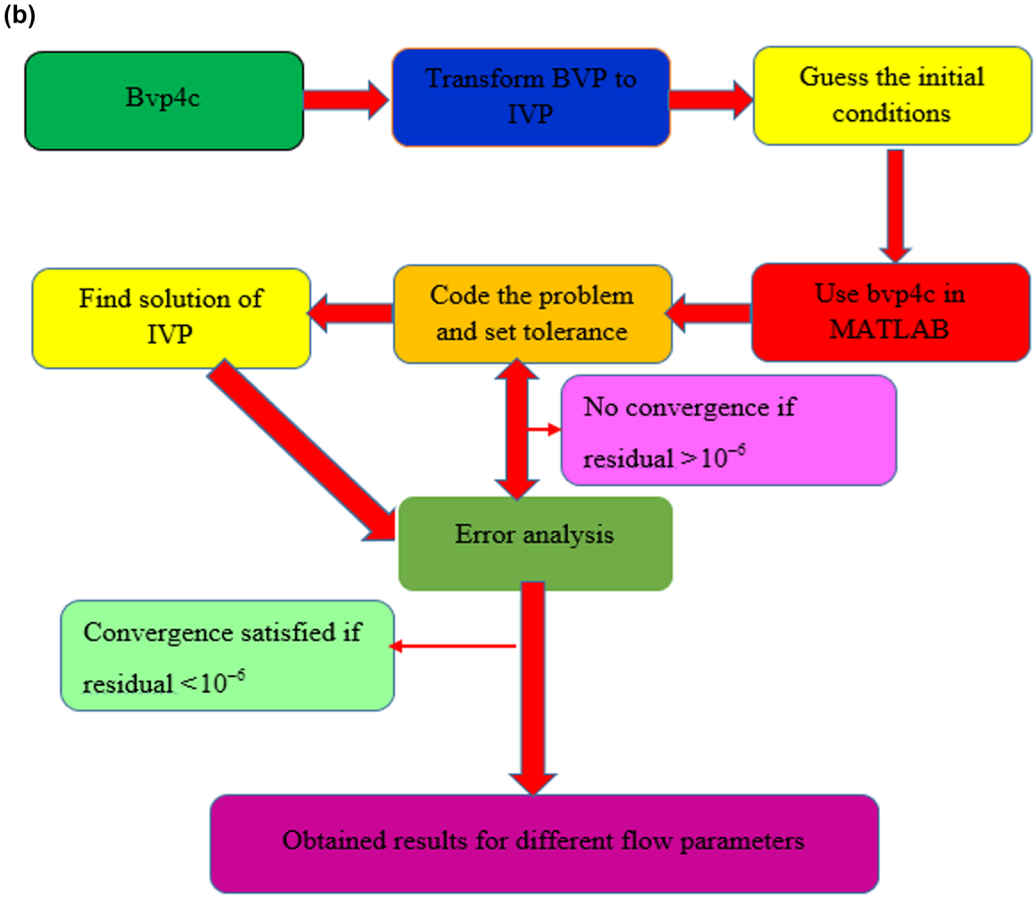

Figure 1: (a) Geometrical representation of the model flow. (b) Numerical scheme.

Table 1: Values of the thermophysical characteristics of nanoparticles and H_2O [59]

Physical properties	Density ($kg\ m^{-3}$)	Heat capacitance j($kg\ K^{-1}$)	Electrical conductivity ($S\ m^{-1}$)	Thermal conductivity $\frac{W}{(m\ K)}$	Thermal expansion coefficient $\frac{1}{(K)}$
H_2O	997.1	4,179	0.05	0.613	21×10^{-6}
SWCNT	2,600	425	10^6	6,600	2.7×10^{-6}
MWCNT	1,600	796	1.9×10^{-4}	3,000	4.4×10^{-6}

$$\Phi'' + \mathrm{Sc}(1+d)f\Phi' - \mathrm{ScKr}(1+\delta\theta)^n \mathrm{Exp}\left(\frac{-E}{(1+\delta\theta)}\right)\Phi = 0. \quad (9)$$

The related boundary conditions are as follows:

$$\left.\begin{aligned} &f'(\xi \to 0) = 1,\ \ f(\xi \to 0) = 0,\ \ \frac{k_{\mathrm{hnf}}}{k_{\mathrm{f}}}\theta'(\xi \to 0) \\ &\quad = \gamma(\theta(\xi \to 0) - 1), \\ &\Phi'(\xi \to 0) = \alpha(\Phi(\xi \to 0) - 1), \\ &\theta(\xi \to \infty) = 0,\ \ \Phi(\xi \to \infty) = 0,\ \ f'(\xi \to \infty) = 0. \end{aligned}\right\} \quad (10)$$

Here, $\mathrm{Pr}\left(=\frac{\upsilon_{\mathrm{f}}(\rho C_{\mathrm{p}})_{\mathrm{f}}}{k_{\mathrm{f}}}\right)$ is the Prandtl number, $\mathrm{Gr}\left(=\frac{gl^2(\widehat{\beta}_{\mathrm{T}})_{\mathrm{f}}(T_{\mathrm{f}} - T_\infty)}{\upsilon_{\mathrm{f}} u_w}\right)$ is the thermal Grashof number, $M\left(=\frac{\sigma_{\mathrm{f}} B_0^2}{\upsilon_{\mathrm{f}}\rho_{\mathrm{f}}}\right)$ is the magnetic factor, $\mathrm{Gc}\left(=\frac{gl^2(\widehat{\beta}_C)_{\mathrm{f}}(C_{\mathrm{f}} - C_\infty)}{\upsilon_{\mathrm{f}} u_w}\right)$ is the solutal Grashof number, $\mathrm{Kr}\left(=\frac{L^2 Q}{\upsilon_{\mathrm{f}}}\right)$ is the chemical reaction, $\delta\left(=\frac{T_w - T_\infty}{T_\infty}\right)$ is the temperature difference, $E\left(=\frac{E_a}{k_a T_\infty}\right)$ is the activation energy, $\mathrm{Ec}\left(=\frac{u_w}{(C_{\mathrm{p}})_{\mathrm{f}}(T_{\mathrm{f}} - T_\infty)}\right)$ is the Eckert number, $\mathrm{Rd}\left(=\frac{4\sigma_* T_\infty^2}{3k_e k_{\mathrm{f}}(T_{\mathrm{f}} - T_\infty)}\right)$ is the thermal radiation, $Q_1\left(=\frac{Q_1 l^2}{\upsilon_{\mathrm{f}}(\rho C_{\mathrm{p}})_{\mathrm{f}}}\right)$ is the heat source, $\mathrm{Sc}\left(=\frac{\upsilon_{\mathrm{f}}}{D_{\mathrm{B}}}\right)$ is Schmidt number, $\gamma\left(=\frac{h_{\mathrm{f}} l^2}{k_{\mathrm{f}}}\right)$ is the thermal Biot number, $\mathrm{Qe}\left(=\frac{Q_2 l^2}{\upsilon_{\mathrm{f}}(\rho C_{\mathrm{p}})_{\mathrm{f}}}\right)$ is a space-dependent heat source, and $\alpha\left(=\frac{h_m l^2}{D_{\mathrm{B}}}\right)$ is the solutal Biot number.

3 Physical quantity of interest

The key engineering aspects, *i.e.*, surface drag, heat transfer rate, and mass number, are given as follows [44]:

Table 2: Thermophysical properties of the models for nano and hybrid nanofluids [44]

Dynamic viscosity	$\frac{\mu_{\mathrm{nf}}}{\mu_{\mathrm{f}}} = \frac{1}{(1-\varphi_{1,2})^{\frac{25}{10}}},\ \ \frac{\mu_{\mathrm{hnf}}}{\mu_{\mathrm{f}}} = \frac{1}{(1-\varphi_1)^{\frac{25}{10}}(1-\varphi_2)^{\frac{25}{10}}}$
Density	$\frac{\rho_{\mathrm{hnf}}}{\rho_{\mathrm{f}}} = (1 - \varphi_{1,2}) + \varphi_{1,2}\frac{\rho_{1,2}}{\rho_{\mathrm{f}}},\ \ \frac{\rho_{\mathrm{hnf}}}{\rho_{\mathrm{f}}} = (1 - \varphi_1 - \varphi_2) + \frac{\rho_1\varphi_1}{\rho_{\mathrm{f}}} + \frac{\rho_2\varphi_2}{\rho_{\mathrm{f}}}$
Heat capacitance	$\frac{(\rho C_{\mathrm{p}})_{\mathrm{hnf}}}{(\rho C_{\mathrm{p}})_{\mathrm{f}}} = (1 - \varphi_{1,2}) + \varphi_{1,2}\frac{(\rho C_{\mathrm{p}})_{1,2}}{(\rho C_{\mathrm{p}})_{\mathrm{f}}},$
	$\frac{(\rho C_{\mathrm{p}})_{\mathrm{hnf}}}{(\rho C_{\mathrm{p}})_{\mathrm{f}}} = (1 - \varphi_1 - \varphi_2) + \frac{(\rho C_{\mathrm{p}})_1\varphi_1}{(\rho C_{\mathrm{p}})_{\mathrm{f}}} + \frac{(\rho C_{\mathrm{p}})_1\varphi_2}{(\rho C_{\mathrm{p}})_{\mathrm{f}}}$
Thermal expansion coefficient	$\frac{(\rho\widehat{\beta})_{\mathrm{nf}}}{(\rho\widehat{\beta})_{\mathrm{f}}} = (1 - \varphi_{1,2}) + \varphi_{1,2}\frac{(\rho\widehat{\beta})_{1,2}}{(\rho\widehat{\beta})_{\mathrm{f}}},$
	$\frac{(\rho\widehat{\beta})_{\mathrm{hnf}}}{(\rho\widehat{\beta})_{\mathrm{f}}} = (1 - \varphi_1 - \varphi_2) + \frac{(\rho\widehat{\beta})_1\varphi_1}{(\rho\widehat{\beta})_{\mathrm{f}}} + \frac{(\rho\widehat{\beta})_2\varphi_2}{(\rho\widehat{\beta})_{\mathrm{f}}}$
Electrical conductivity	$\frac{\sigma_{\mathrm{nf}}}{\sigma_{\mathrm{f}}} = 1 + \frac{3\left(\frac{\sigma_{1,2}}{\sigma_{\mathrm{f}}} - 1\right)\varphi_{1,2}}{\left(\frac{\sigma_{1,2}}{\sigma_{\mathrm{f}}} - 2\right) - \left(\frac{\sigma_{1,2}}{\sigma_{\mathrm{f}}} - 1\right)\varphi_{1,2}}$
	$\frac{\sigma_{\mathrm{hnf}}}{\sigma_{\mathrm{f}}} = \frac{\frac{\sigma_1\varphi_1 + \sigma_2\varphi_2}{\varphi_1 + \varphi_2} + 2\sigma_{\mathrm{f}} + 2(\sigma_1\varphi_1 + \sigma_2\varphi_2) - 2(\varphi_1 + \varphi_2)\sigma_{\mathrm{f}}}{\frac{\sigma_1\varphi_1 + \sigma_2\varphi_2}{\varphi_1 + \varphi_2} + 2\sigma_{\mathrm{f}} - (\sigma_1\varphi_1 + \sigma_2\varphi_2) + (\varphi_1 + \varphi_2)\sigma_{\mathrm{f}}}$
Thermal conductivity	$\frac{k_{\mathrm{nf}}}{k_{\mathrm{f}}} = 1 + \frac{3\left(\frac{k_{1,2}}{k_{\mathrm{f}}} - 1\right)\varphi_{1,2}}{\left(\frac{k_{1,2}}{k} - 2\right) - \left(\frac{k_{1,2}}{k} - 1\right)\varphi_{1,2}}$
	$\frac{k_{\mathrm{hnf}}}{k_{\mathrm{f}}} = \frac{\frac{k_1\varphi_1 + k_2\varphi_2}{\varphi_1 + \varphi_2} + 2k_{\mathrm{f}} + 2(k_1\varphi_1 + k_2\varphi_2) - 2(\varphi_1 + \varphi_2)k_{\mathrm{f}}}{\frac{k_1\varphi_1 + k_2\varphi_2}{\varphi_1 + \varphi_2} + 2k_{\mathrm{f}} - (k_1\varphi_1 + k_2\varphi_2) + (\varphi_1 + \varphi_2)k_{\mathrm{f}}}$

$$\left.\begin{aligned} C_{fx} &= \frac{\mu_{\mathrm{hnf}}}{\rho_{\mathrm{f}} u_w^2}\frac{\partial u}{\partial y}, \quad \mathrm{Sh}_x = \frac{-xD_{\mathrm{B}}}{D_{\mathrm{B}}(C_{\mathrm{f}} - C_\infty)}\frac{\partial C}{\partial y}, \\ \mathrm{Nu}_x &= \frac{-x}{k_{\mathrm{f}}(T_{\mathrm{f}} - T_\infty)}\left(k_{\mathrm{hnf}} + \frac{16\sigma_* T_\infty^3}{3k_e}\right)\frac{\partial T}{\partial y}. \end{aligned}\right|_{\text{at } y=0} \tag{11}$$

Eq. (11) is reduced to the non-dimensional form using Eq. (6):

$$\left.\begin{aligned} C_{fx}(R_d)^{-1/2} &= \frac{\mu_{\mathrm{hnf}}}{\mu_{\mathrm{f}}} f''(0), \quad \mathrm{Sh}_x(R_d)^{1/2} = -\Phi'(0), \\ \mathrm{Nu}_x(R_d)^{1/2} &= -\left(\frac{k_{\mathrm{hnf}}}{k_{\mathrm{f}}} + \frac{4}{3}\mathrm{Rd}\right)\theta'(0). \end{aligned}\right| \tag{12}$$

4 Numerical scheme

The non-dimensional equations were numerically solved along with the accompanying boundary conditions by using the built-in function bvp4c in the MATLAB package. The resolution of BVPs in the bvp4c method in MATLAB provides a number of advantages compared to other approaches. The versatility is one of the notable strengths of bvp4c; it is suited for managing a wide range of linear and non-linear BVPs generated by various scientific and engineering applications. Accurate and stable solutions can be obtained by employing a collocation technique that discretizes the problem domain into a set of collocation points. This helps maximize the use of computational resources through optimization. Furthermore, bvp4c is a user-friendly interface that simplifies the creation of complex BVPs. The bvp4c is a better tool of choice due to its versatility, robustness, and efficiency for solving a number of BVPs. To convert the ODEs into a set of first-order differential equations, the following terms are incorporated into the given equations:

Let

$$\left.\begin{aligned} &\mathfrak{R}_1 = f(\xi), \quad \mathfrak{R}_2 = f'(\xi), \quad \mathfrak{R}_3 = f''(\xi), \\ &\mathfrak{R}_3' = f'''(\xi), \quad \mathfrak{R}_4 = \theta(\xi), \quad \mathfrak{R}_5 = \theta'(\xi), \\ &\mathfrak{R}_5' = \theta''(\xi), \quad \mathfrak{R}_6 = \Phi(\xi), \quad \mathfrak{R}_7 = \Phi'(\xi), \\ &\mathfrak{R}_7' = \Phi''(\xi). \end{aligned}\right| \tag{13}$$

Using the substation given in Eq. (13), the following set of first-order differential equations is obtained:

$$\begin{aligned} \mathfrak{R}_3' = {} & \frac{(\rho_{\mathrm{hnf}}/\rho_{\mathrm{f}})}{(\mu_{\mathrm{hnf}}/\mu_{\mathrm{f}})}\{y(2)^2 - (1+d)y(1)y(3)\} \\ & + \frac{(\sigma_{\mathrm{hnf}}/\sigma_{\mathrm{f}})}{(\mu_{\mathrm{hnf}}/\mu_{\mathrm{f}})}My(2) - \frac{((\rho\widehat{\beta})_{\mathrm{hnf}}/(\rho\widehat{\beta})_{\mathrm{f}})}{(\mu_{\mathrm{hnf}}/\mu_{\mathrm{f}})}(\mathrm{Gr}y(4) \\ & + \mathrm{Gc}y(6))\mathrm{Cos}\,\alpha, \end{aligned} \tag{14}$$

$$\begin{aligned} \mathfrak{R}_5' = -\mathrm{Pr}\Bigg\{ & Q_1 y(4) + \frac{(\rho C_{\mathrm{p}})_{\mathrm{hnf}}}{(\rho C_{\mathrm{p}})_{\mathrm{f}}}(1+d)y(1)y(5) \\ & + Q_e\mathrm{Exp}(-m\xi) + \frac{\sigma_{\mathrm{hnf}}}{\sigma_{\mathrm{f}}}\mathrm{MEc}y(2)y(2)\Bigg\}, \end{aligned} \tag{15}$$

$$\begin{aligned} \mathfrak{R}_7' = -\mathrm{Sc}\Bigg\{ & (1+d)y(1)y(7) - \mathrm{Kr}(1+\delta y(4))\mathrm{Exp}\Bigg(\\ & -\frac{E}{1+\delta y(4)}\Bigg)y(6)\Bigg\}. \end{aligned} \tag{16}$$

The boundary constraints are as follows:

$$\left.\begin{aligned} &\mathfrak{R}_2(a) - 1, \quad \mathfrak{R}_1(a) - 0, \quad \mathfrak{R}_2(b) - 0, \\ &\frac{k_{\mathrm{hnf}}}{k_{\mathrm{f}}}\mathfrak{R}_5(a) - \gamma(\mathfrak{R}_4(a) - 1), \quad \mathfrak{R}_4(b) - 0, \\ &\mathfrak{R}_7(a) - \alpha(\mathfrak{R}_6(a) - 1), \quad \mathfrak{R}_6(b) - 0. \end{aligned}\right| \tag{17}$$

Table 3: Ranges and default values of the physical parameters

Parameters	Default values	Ranges
M	0.1	$0.0 \le M \le 5.0$
Gr	0.1	$0.2 \le \mathrm{Gr} \le 2.0$
Gc	0.1	$0.1 \le \mathrm{Gc} \le 3.0$
Rd	0.2	$0.3 \le \mathrm{Rd} \le 1.5$
Ec	0.1	$0.2 \le \mathrm{Ec} \le 1.5$
Pr	6.2	$0.1 \le \mathrm{Pr} \le 1.0$
Q_1	0.1	$0.1 \le Q_1 \le 0.5$
Qe	0.1	$0.4 \le Q_1 \le 0.6$
γ	0.1	$0.4 \le \gamma \le 1.5$
Sc	2.0	$0.3 \le \mathrm{Sc} \le 1.4$
Kr	0.2	$0.2 \le \mathrm{Kr} \le 3.0$
E	0.1	$1.0 \le E \le 3.0$
α	0.1	$0.3 \le \beta \le 3.0$
φ_1, φ_2	0.04	$0.01 \le (\varphi_{1,2}) \le 0.04$
d	1.0	$0.0 \le d \le 1.0$

5 Validation

The validation of this study with the already published work of Palani *et al.* [60] and Kumar *et al.* [61], utilizing the bvp4c technique, is presented in Table 4. The strong alignment between the findings of the current and prior studies validates the accuracy of the model and method. Figure 2(a) and (b) shows a graphical comparison of the present work with Palani *et al.* [60]. and Kumar *et al.* [61] and found excellent agreement between them.

Table 4: Validation of this study with the work of Palani *et al.* [60] and Kumar *et al.* [61] for different values of Pr

Pr	Skin friction			Nusselt number		
	Palani *et al.* [60]	Kumar *et al.* [61]	Present outcomes	Palani *et al.* [60]	Kumar *et al.* [61]	Present outcomes
0.1	1.10236	1.10235	1.10242	0.20922	0.20922	0.20931
0.7	0.82566	0.82567	0.82623	0.44771	0.44770	0.44781
1.0	0.77524	0.77524	0.77526	0.50670	0.50671	0.50675

6 Results and discussion

This section presents a graphical representation of the key parameters influencing the associated profiles. The effect of the emerging factors such as the thermal Grashof number (Gr), the magnetic factor (M), the solutal Grashof number (Gc), the chemical reaction (Kr), the acti-

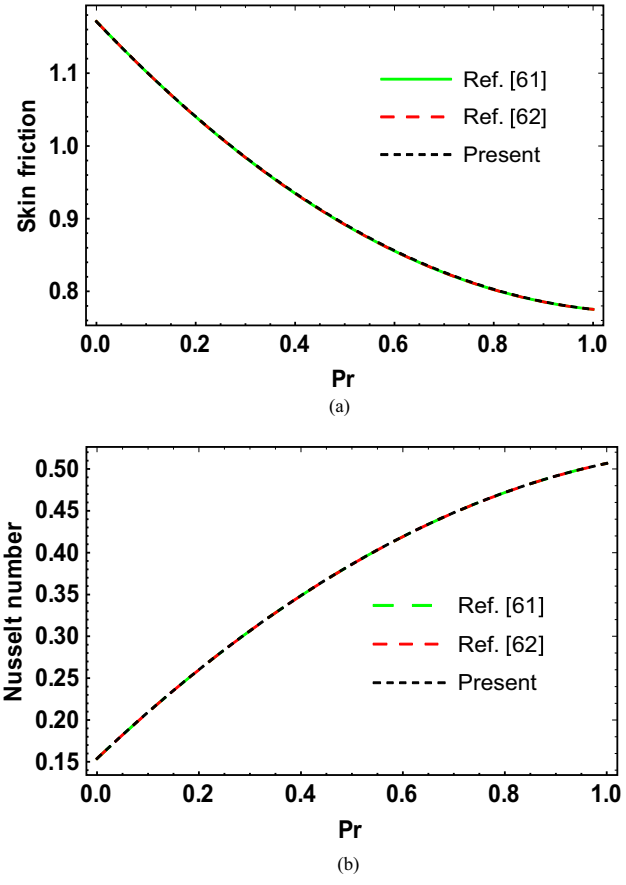

Figure 2: (a) and (b) Comparison of the skin friction and Nusselt number values for varying Pr numbers.

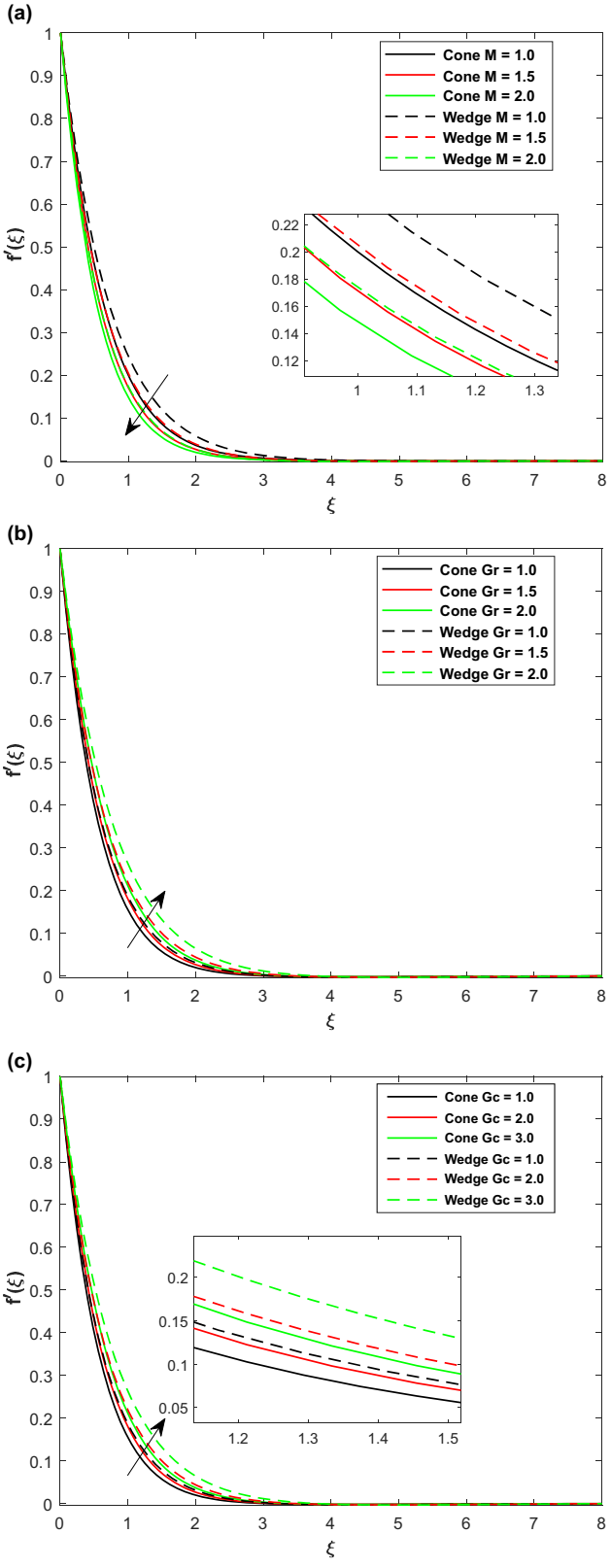

Figure 3: (a) $f'(\xi)$ corresponding to varying M. (b) $f'(\xi)$ corresponding to varying Gr. (c) $f'(\xi)$ corresponding to varying Gc.

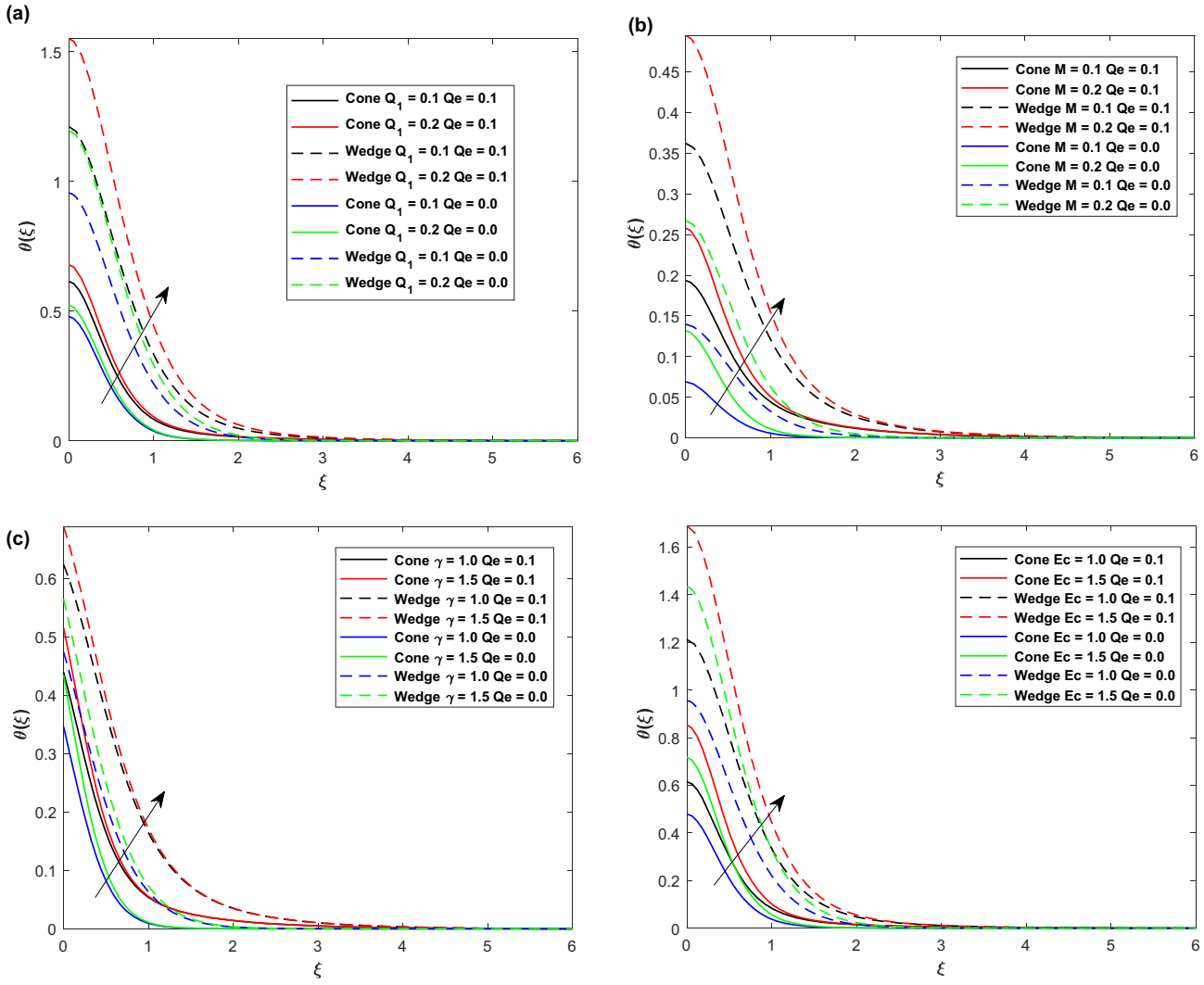

Figure 4: (a) $\theta(\xi)$ corresponding to varying Q_1. (b) $\theta(\xi)$ corresponding to varying M. (c) $\theta(\xi)$ corresponding to varying γ. (d) $\theta(\xi)$ corresponding to varying Ec.

vation energy (E), the Eckert number (Ec), the thermal radiation (Rd), the heat source (Q_1), the Schmidt number (Sc), the thermal Biot number (γ), the space-dependent heat source (Qe), and (λ) the solutal Biot number on velocity $f'(\xi)$, temperature $\theta(\xi)$, and concentration $\Phi(\xi)$ distributions are shown in Figures 3–5. The influence on the key physical quantities, including the skin friction $C_{fx}(R_d)^{-1/2}$, Nusselt $\mathrm{Nu}_x(R_d)^{1/2}$, and Sherwood number $\mathrm{Sh}_x(R_d)^{1/2}$, are presented in Figures 6–10. Table 1 outlines the thermophysical values of SWCNT, MWCNT, and the base fluid. The theoretical models for the thermophysical characteristics are displayed in Table 2. The range of physical parameters is given in Table 3. The validation of the current model against previously reported results is presented in Table 4. Figure 1(a) shows the physical mechanism of the model, and Figure 1(b) shows the mechanism of the numerical scheme. Figure 2(a) and (b) shows the graphical comparison of the present work with Palani *et al.* [60] and Kumar *et al.* [61]. The effect of varying M on $f'(\xi)$ distributions is shown in Figure 3(a). According to Figure 3(a), the $f'(\xi)$ profiles of the hybrid nanofluid decreased as M increased. Physically, the enhancement of M produced a kind of resistive force known as the Lorentz force. This Lorentz force is felt by the charged particles when they travel through a magnetic field. The level and direction of the Lorentz force depend on the charge of the particle, velocity, strength, and direction of the magnetic field. Assuming no change in the field direction, a larger magnetic field exerts a greater force on the charged particle, causing the fluid's velocity to decrease. The velocity of the cone decreased more than the wedge velocity in the present study. Figure 3(b) shows the effect of Gr on the $f'(\xi)$ field for both the cone and wedge. It has been noted that the $f'(\xi)$ profile

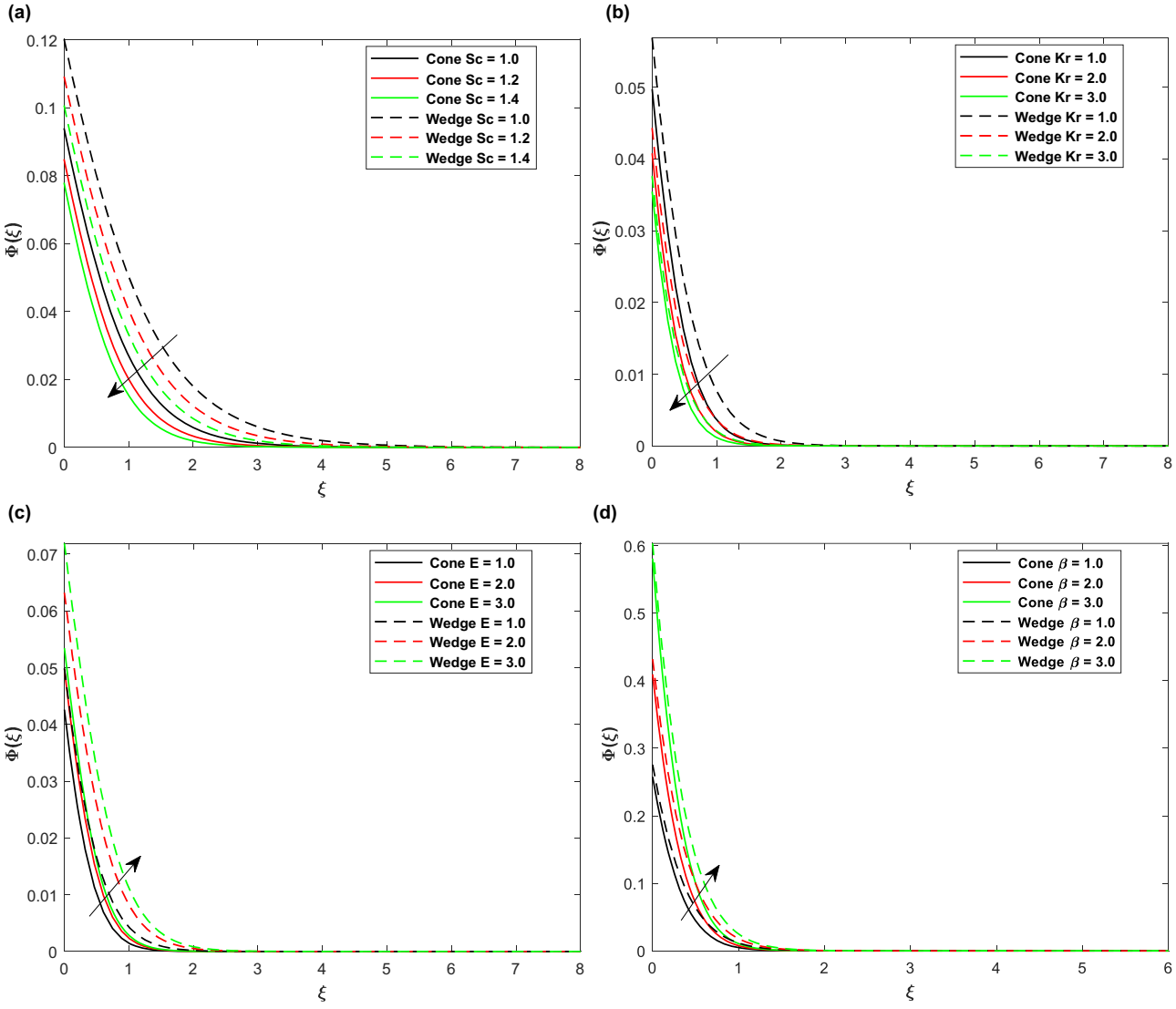

Figure 5: (a) $\Phi(\xi)$ corresponding to varying Sc. (b) $\Phi(\xi)$ corresponding to varying Kr. (c) $\Phi(\xi)$ corresponding to varying E. (d) $\Phi(\xi)$ corresponding to varying α.

increased with increasing Gr. The main reason is that $\mathrm{Gr}\left(=\frac{gl^2(\widehat{\beta}_T)_f(T_f - T_\infty)}{\upsilon_f u_w}\right)$ is inversely linked to viscosity. Therefore, the higher values of Gr are associated with a decrease in the viscosity of the hybrid nanofluid. Thus, the $f'(\xi)$ profile increased with decreasing viscosity parameter. Furthermore, the cone elicits a more pronounced impression than the wedge. Figure 3(c) shows the impact of Gc on $f'(\xi)$. Gc exhibits a similar behavior to that of Gr in this context. The consequences of Gr and Gc on $f'(\xi)$ are similar to the results of Dawar *et al.* [24]. Moreover, Gr and Gc are related to the buoyancy force. Therefore, when they increase, the buoyancy force also increases. Hence, the $f'(\xi)$ profile also increases. The study's findings show that the improvement in both thermal and mass Grashof numbers increased the velocity profile, supporting the effectiveness of hybrid nanofluids in cooling technologies for electronic devices. Figure 4(a) shows the impact of Q_1 on $\theta(\xi)$ for both the Qe = 0.1 and Qe = 0.0 scenarios. For both the cone and wedge, the graph demonstrates that the $\theta(\xi)$ curves have an upward trend as Q_1 increases. It is noticed that $\theta(\xi)$ increases as a result of both Q_1 and Qe. Physically, the combined effect of Q_1 and Qe produces more heat within the fluid system due to which the $\theta(\xi)$ profile increases. When both Q_1 and Qe are present, the thermal field is significantly higher for the wedge geometry than for the cone geometry. It is essential to recognize that the exponential heat source Qe is significantly more important than Q_1. Furthermore, the influence of Q_1 increases when Qe = 0.1 compared to Qe = 0.0. Figure 4(b) shows the variation of M on the $\theta(\xi)$ profile for two distinct geometries

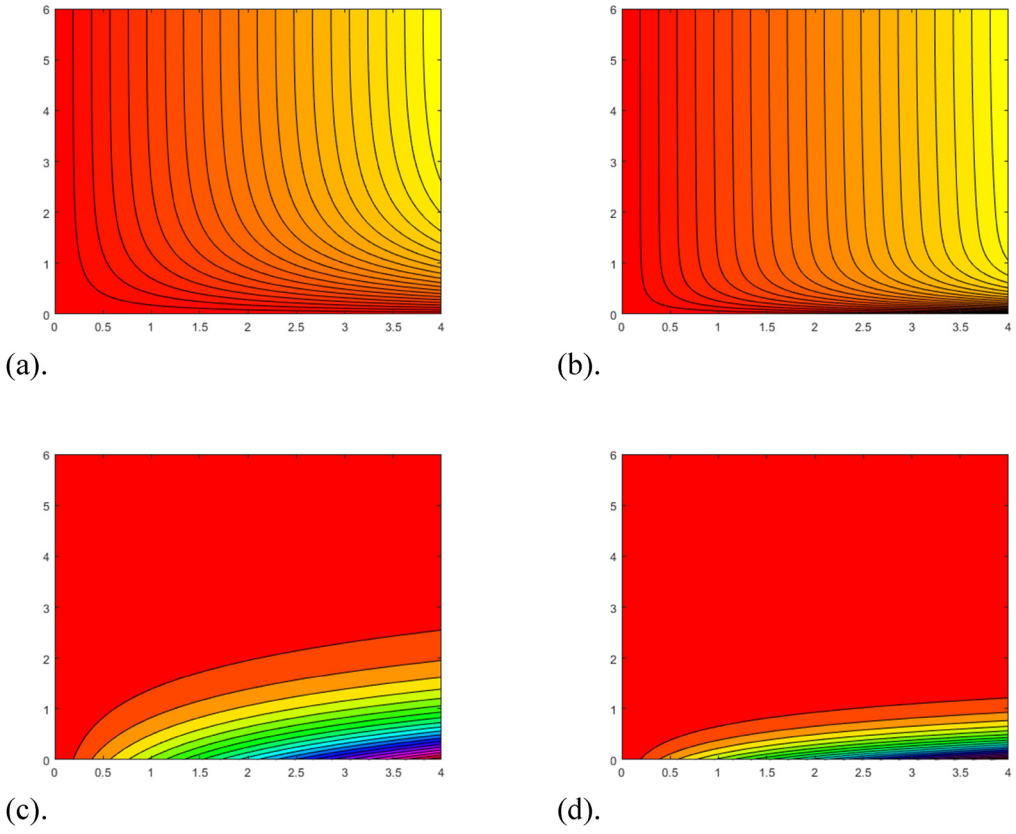

Figure 6: (a)–(d) Streamlines and contours plates for the cone surface when $M = 0$ and $M = 5.0$.

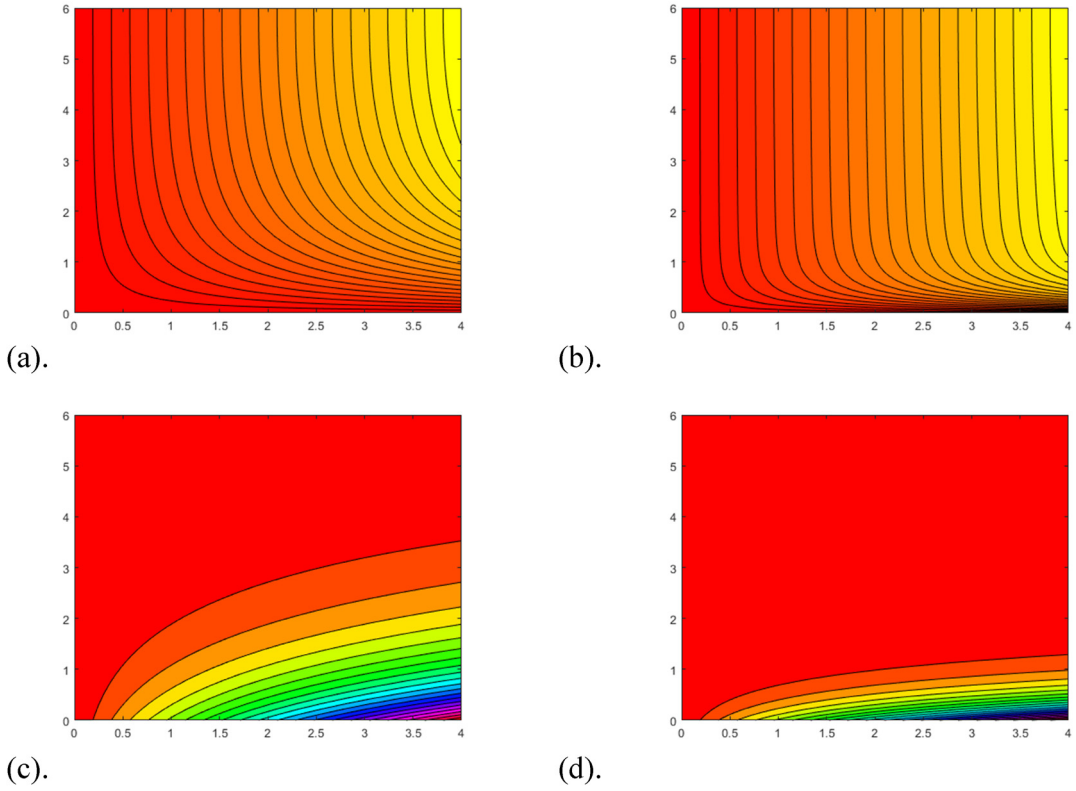

Figure 7: (a)–(d) Streamlines and contours plates for the wedge surface when $M = 0$ and $M = 5.0$.

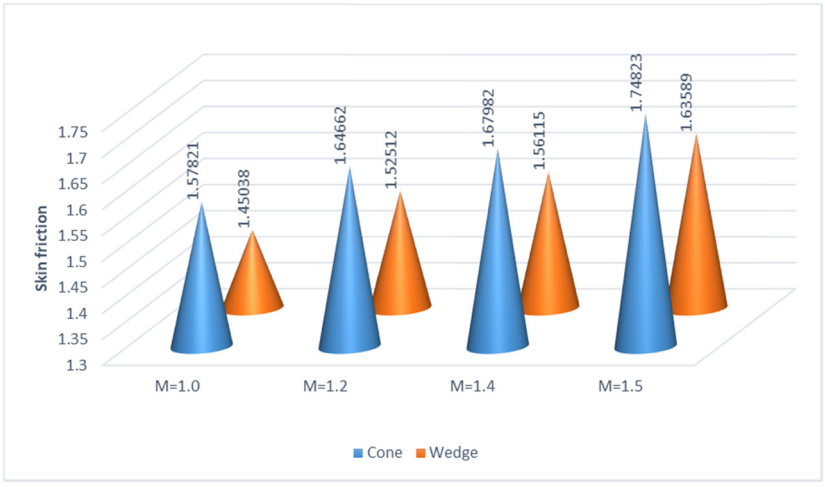

(a)

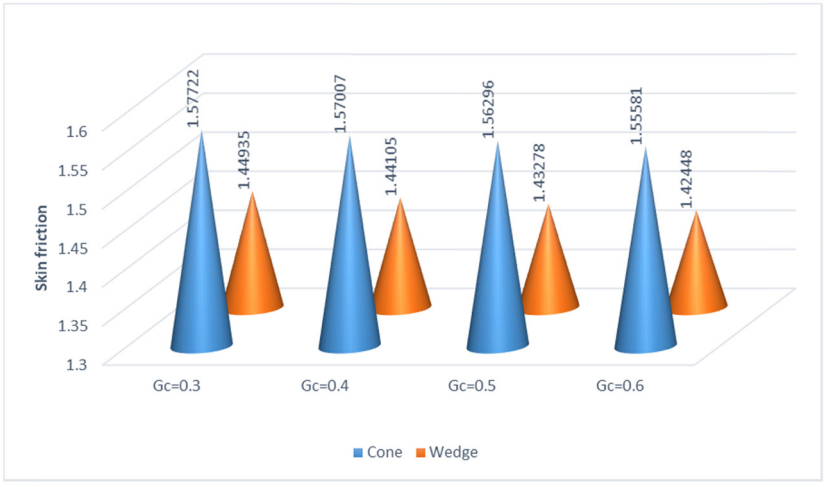

(b)

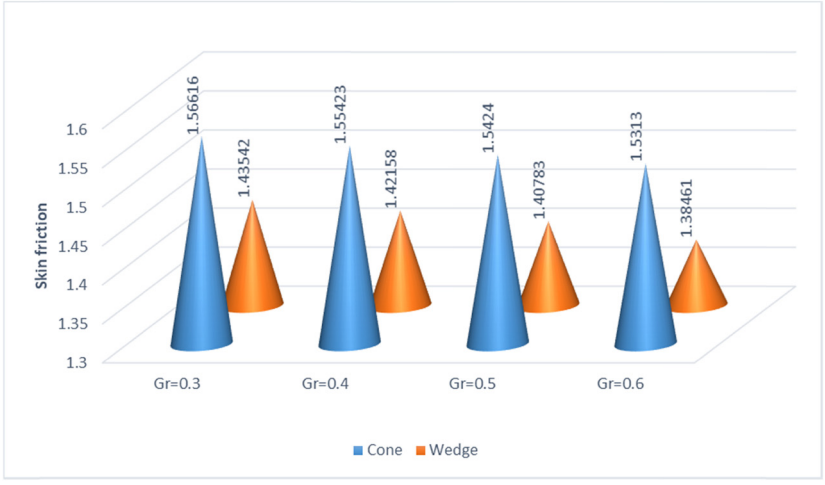

(c)

Figure 8: (a)–(c) Variation in the skin frictions of the cone and wedge for various values of M, Gc, and Gr.

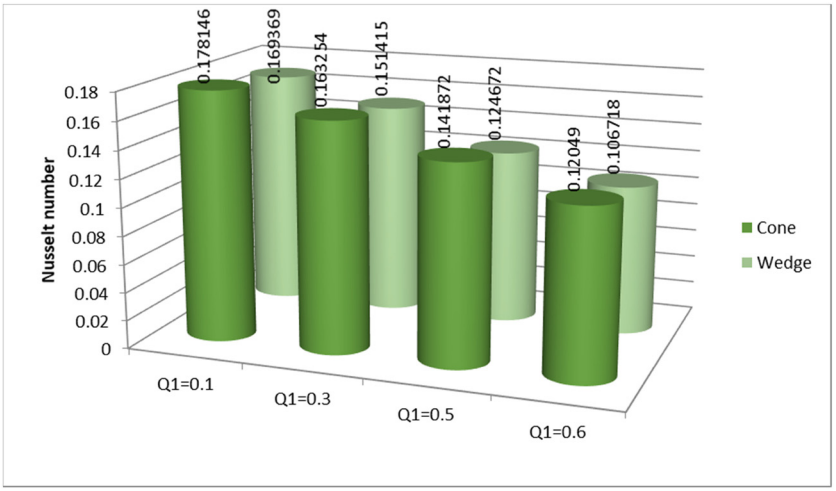

(a)

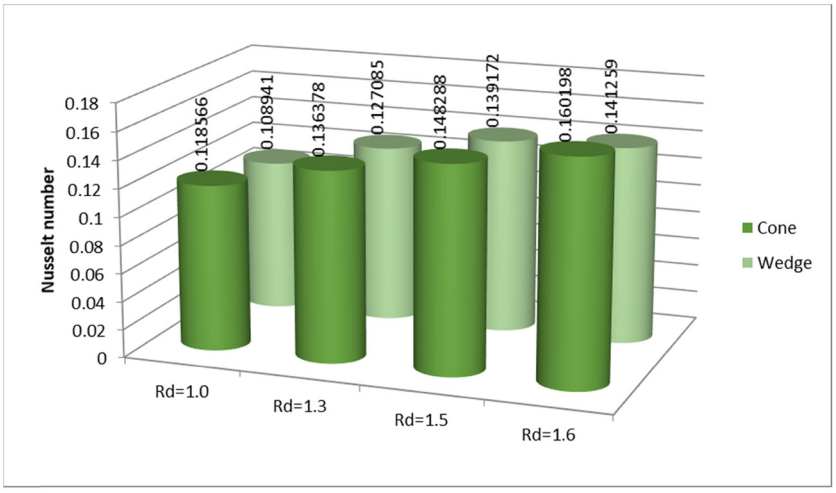

(b)

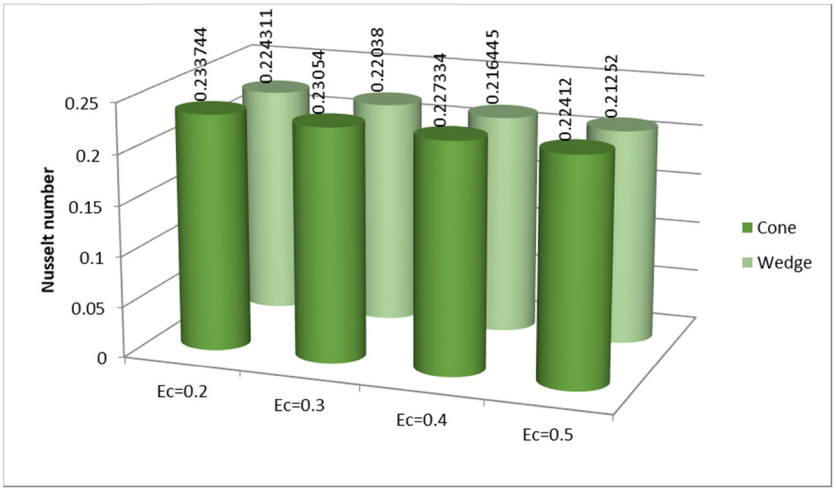

(c)

Figure 9: (a)–(e) Influence of Q_1, Rd, Ec, and γ on the Nusselt number for the cone and wedge.

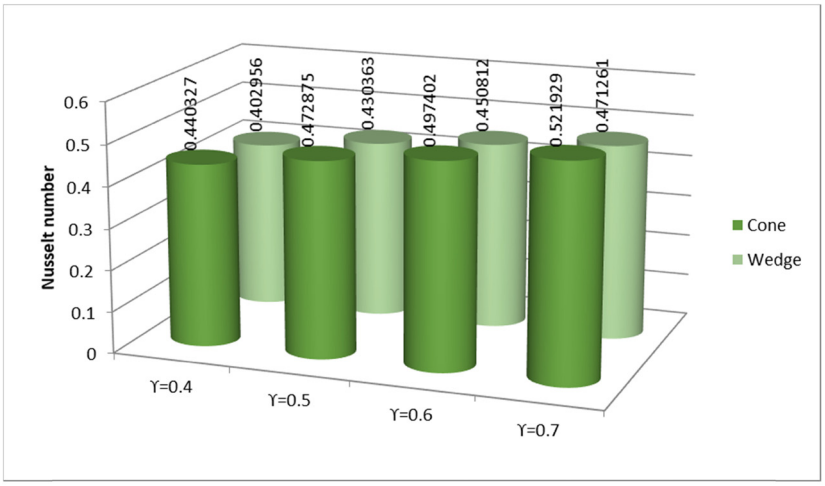

(d)

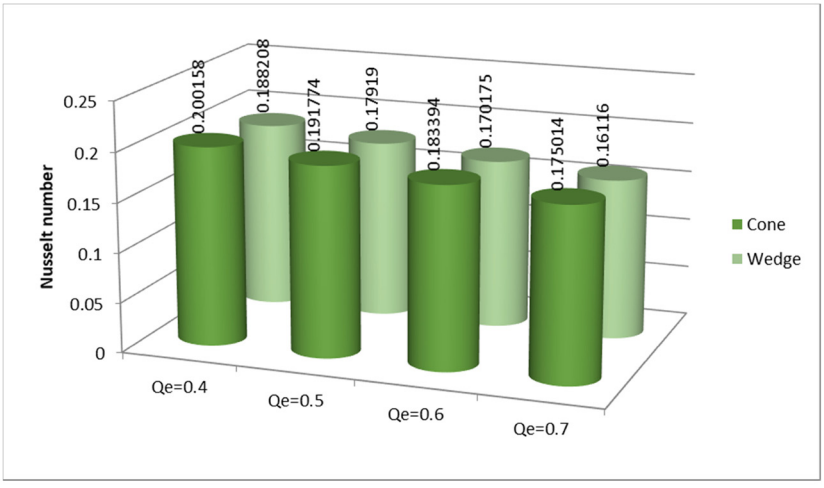

(e)

Figure 9: (*Continued*)

(cone and wedge) when Qe = 0.1 and Qe = 0.0. When the values of M increased, it is clear that the $\theta(\xi)$ profile for the two distinct geometries increased. Physically, the increase in M produces an opposing force called the Lorentz force, which is applied to the fluid. This Lorentz force on the velocity profiles generates a certain form of friction in the flow. Consequently, the velocity of the fluid begins to decrease. This friction between the fluid particles and surface is enhanced, which generates more heat energy, as a result, the $\theta(\xi)$ distribution gradually increases. This increment in $\theta(\xi)$ is more pronounced for the wedge with the space-based heat source Qe = 0.1. The effect of γ on the $\theta(\xi)$ profile for both cone and wedge geometries is depicted in Figure 4(c). Increasing amounts of γ significantly improve the $\theta(\xi)$ profile. A dimensionless variable known as the Biot number $\gamma\left(=\frac{l^2 h_f}{k_f}\right)$ can be used to determine the thermal convective limitation for heat transfer; this number is the ratio of convection and conduction of heat between the solid body and the adjacent fluid. Here, (h_f) represents the nanofluid's heat transfer coefficient and (k_f) stands for its thermal conductivity. This is based on the fact that the strength of convective heating is directly related to γ. When γ increased, greater amount of heat is transferred from the heated surface to the boundary layer fluid. Thus, the thermal $\theta(\xi)$ profile increases. This increase in the $\theta(\xi)$ profile is more significant for the wedge geometry when Qe = 0.1. Figure 4(d) shows the influence of Ec on the $\theta(\xi)$ profile for both cone and wedge geometries for Qe = 0.1 and Qe = 0.0. It is noticed that with the enrichment of Ec, the $\theta(\xi)$ profile of the hybrid nanofluid improves for both the cone and wedge surfaces. The Ec, also known as the viscous dissipation factor, is a measure of the amount of energy that

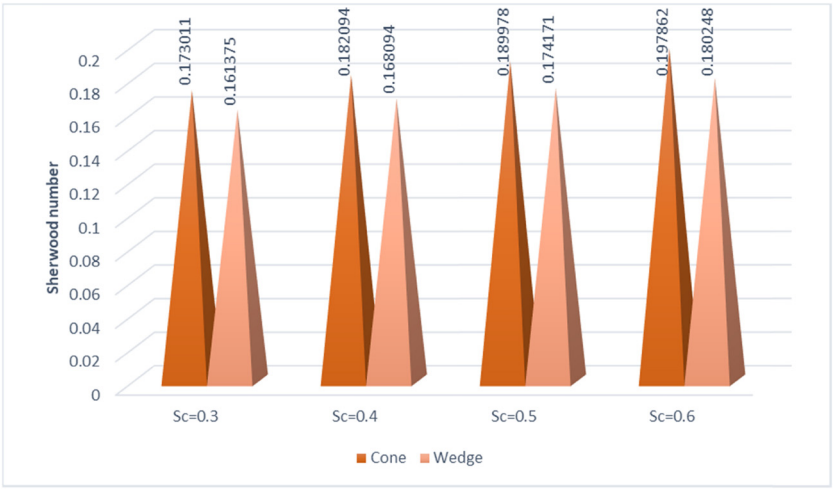

(a)

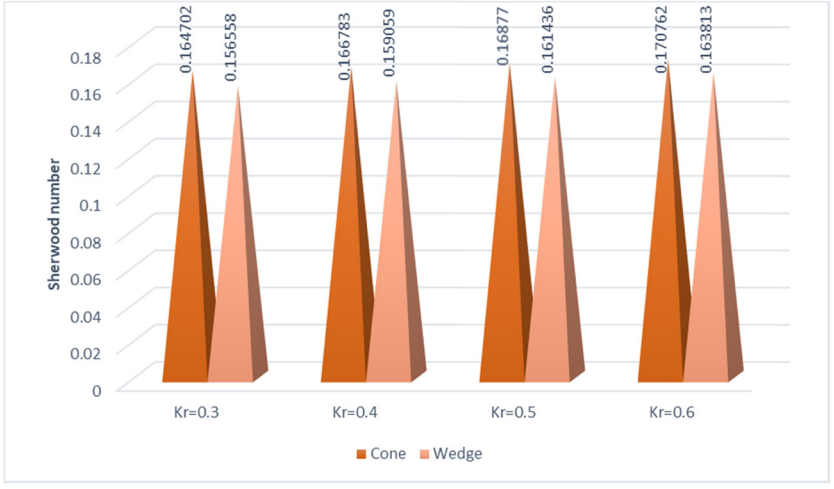

(b)

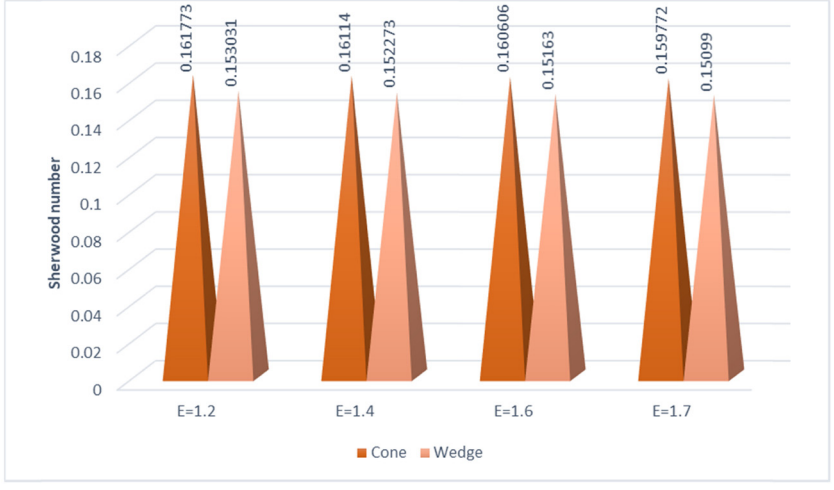

(c)

Figure 10: (a)–(d) Influence of Sc, Kr, E, and α on the Sherwood number for the cone and wedge.

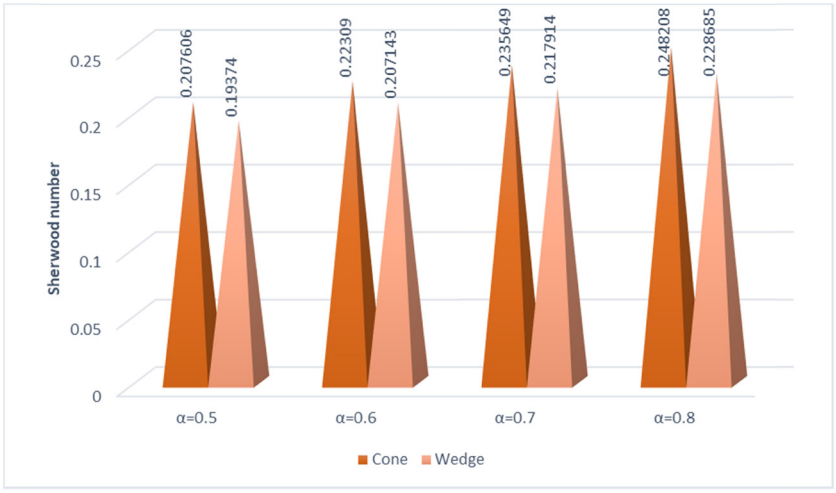

(d)

Figure 10: (*Continued*)

is lost by a fluid as a result of various frictional forces within the fluid. There is a strong connection between the viscosity of the fluid and the velocity gradient. In the context of heat transmission, the significance of the energy dissipation is described by the viscous dissipation parameter. When Ec is increased, it indicates that there is a greater amount of energy loss and heating occurs within the fluid. Thus, the $\theta(\xi)$ distribution becomes higher. The effects of Sc on $\Phi(\xi)$ are depicted in Figure 5(a). The $\Phi(\xi)$ contour becomes less prominent for both cones and wedges as Sc increases. $\mathrm{Sc}\left(=\frac{\upsilon_{\mathrm{f}}}{D_{\mathrm{B}}}\right)$ is a dimensionless number related to the viscosity and diffusion coefficient. If the value of Sc is larger, it suggests that υ_{f} is more widespread than D_{B}. The process of mass diffusion is related to the transfer of mass (concentration) of a specific substance, whereas momentum diffusion is linked to the transfer of momentum within the fluid containing the substance. When Sc is high, the behavior of the flow is determined more by the velocity field than the mass diffusion. This indicates that the fluid is more effective at conveying momentum than mass diffusion. The concentration gradients are less prominent than the velocity gradients, which leads to a thinner concentration boundary layer near the surface. Therefore, $\Phi(\xi)$ declines with higher Sc. The decreasing effect of $\Phi(\xi)$ is more for cones, as shown in Figure 4(a). The influence of Kr on $\Phi(\xi)$ is shown in Figure 5(b). The deterioration of the concentration field as well as the solutal layer is investigated. Physically, the solutal layer becomes thicker as a result of higher estimation of the variation in the chemical process. The $\Phi(\xi)$ profile thus decreases with the growing estimation of Kr. Figure 5(c) illustrates the effect of E on the $\Phi(\xi)$ distribution. An increasing trend in $\Phi(\xi)$ is observed for higher values of E for both geometries. Physically, when the activation energy increases, the reaction rate decreases, decreasing the chemical process. This reduction improves the concentration profile by promoting the generative chemical reaction, leading to higher $\Phi(\xi)$ profile. This increase in the $\Phi(\xi)$ profile for wedges is more prominent. Figure 5(d) shows the impact of α on the $\Phi(\xi)$ field for cone and wedge geometries. Higher values of α improves the $\Phi(\xi)$ profile for both scenarios (cones and wedges). Physically, $\alpha\left(=\frac{h_m l^2}{D_{\mathrm{B}}}\right)$ is associated with the mass transfer coefficient, which improves with the increasing estimation of β. Higher values of the Biot number strengthens the mass transfer rate, as shown in Figure 7, enhancing the diffusion of species into the fluid. As a result, the $\Phi(\xi)$ field enhances with an increase in α. Consequently, the $\Phi(\xi)$ profile increases. Furthermore, the results reveal that the presence of non-linear heat source tends to intensify the thermal profiles for wedges more significantly as compared to flow over cones, also related to solar power collectors' applications. Figure 6(a)–(d) shows the consequences of M = 0.0 and M = 5.0 toward the cone streamlines and contour plots. It is noted that with flow toward the cone, the streamlines increase due to the improved values of M, whereas the contour plots are narrow. The streamlines and contour plots for the wedge flow also depict the same effect, as shown in Figure 7(a)–(d). Figure 8(a)–(d) shows the mechanism of varying non-dimensional factors M, Gc, and Gr on skin friction for both flow cases (cones and wedges). It is noted that the skin friction is elevated with increasing M for the two geometries. Additionally, compared to the wedge flow, the flow over the cone surface has maximum skin friction. Physically, the magnetic field

increases the Lorentz force, which resists the fluid motion and enhances the resistance. This leads to a greater velocity gradient at the surface, thereby accelerating the skin friction coefficient, as shown in Figure 8(a). Furthermore, the skin friction is decreased for Gc and Gr numbers. This is because the thermal and mass Grashof number enhances the buoyancy forces, which promote the fluid motion, as shown in Figure 3(b) and (c). This increase in the fluid motion leads to a reduction in the skin friction coefficient, as shown in Figure 8(b) and (c). The effects of Q_1, Rd, γ, and Qe on the Nusselt number are shown in Figure 9(a)–(c). From this figure, it is clear that the increase in Q_1 and Qe reduces the temperature gradient at the surface. This weakens the heat transfer rate, leading to a lower Nusselt number. Furthermore, a higher Rd supplied more energy to the system, which raises the temperature gradient at the surface, leading to enhanced Nusselt number. The Biot number (γ) enhances the convective heat transfer at the surface; as a result, the rate of heat transfer is improved. The variation in the Sherwood number for both flows (cones and wedges) *versus* Sc, Kr, E, and α is shown in Figure 10(a)–(d). This figure shows that the Sherwood number increases with increasing Sc. Physically, higher values of the Schmidt number reduce mass diffusivity, improving the concentration gradient at the surface and increasing the Sherwood number. The increase in Kr accelerates species depletion, whereas the reverse impact was observed in the case of activation energy due to reducing species. Physically, α is associated with the mass transfer coefficient, which expands with the increasing values of α. Higher values of the concentration Biot number reinforce the mass transfer rate due to the enhancement of the diffusion of species into the fluid. The observed trends in the mass transfer rate also support filtration and separation technologies, optimizing their efficiency based on the fluid and material properties.

7 Conclusion

In this study, we investigated the MHD hybrid two-dimensional nanofluid flow across two geometries: (a) cones and (b) wedges. To form a hybrid nanofluid, the nanomaterial CNTs were dispersed in water. The temperature equation was modified by incorporating Joule heating, an exponential space-based heat source. Moreover, the Arrhenius energy function is incorporated in the concentration equation. These equations were then transformed into the coupled systems of ODEs and solved by utilizing the bvp4c technique in the MATLAB package. The effects of various flow factors on different flow profiles are summarized as follows:

a) The reducing impression in the skin friction coefficient against higher thermal and mass Grashof numbers is more significant for the wedge geometry, whereas, for the cone geometry, it is improved with the magnetic parameter.
b) The reducing impact of the magnetic field on the velocity profile is higher for the cone as compared to the wedge, whereas an opposite behavior for the temperature profile is found. The increment in the thermal distribution is maximum in the presence of an exponential heat source.
c) The increasing values of the thermal and mass Grashof numbers improved the velocity curves for the cone and wedge. The amplification is higher for the wedge case.
d) The temperature distribution exhibits an increasing trend expansion against the increasing estimation of the Eckert number, thermal radiation, and thermal Biot number, both in the presence and absence of the space-based heat source for the cone and wedge. Moreover, it is noticed that the thermal curves are higher for the wedge when the space-based heat source is present.
e) The concentration distribution for the hybrid nanofluid across a cone drops quicker for varying Schmidt number and the chemical reaction due to the enhancement in molecular diffusivity, while it increases for the activation energy and concentration Biot numbers for the wedge.
f) The rate of heat transfer for the cone surface is higher than the wedge due to the higher values of radiation and Biot number. Moreover, the Nusselt number declined for the Eckert number, thermal, and space-based heat sources.
g) A decrease in performance is noted in the Sherwood number for both surfaces when the Schmidt number, chemical reaction, and solutal Biot number are enhanced, while opposite trends were observed for the activation energy. Furthermore, an increased mass transfer is noticed for cone geometry.
h) The streamlines increase for a higher magnetic field, while contour plots become narrow, for both cone and wedge geometries.

8 Future work

1) Future studies can extend this work by investigating different non-Newtonian models such as Casson and Maxwell models, which are particularly relevant in industrial and biomedical applications.
2) Another potential direction is analyzing the hybrid nanofluid flow in porous media, which is crucial in filtration and oil recovery applications.

3) This study further extends by considering different nanoparticles and boundary conditions.
4) The integration of AI-based models to predict and optimize heat transfer performance in hybrid nanofluid systems.

Acknowledgments: This work was supported by the Deanship of Scientific Research, Vice Presidency for Graduate Studies and Scientific Research, King Faisal University, Saudi Arabia (Grant No. KFU252587) and Princess Nourah bint Abdulrahman University Researchers Supporting Project number (PNURSP2025R183), Princess Nourah bint Abdulrahman University, Riyadh, Saudi Arabia.

Funding information: This work was supported by the Deanship of Scientific Research, Vice Presidency for Graduate Studies and Scientific Research, King Faisal University, Saudi Arabia (Grant No. KFU252587), and Princess Nourah bint Abdulrahman University Researchers Supporting Project number (PNURSP2025R183), Princess Nourah bint Abdulrahman University, Riyadh, Saudi Arabia.

Author contributions: All authors have accepted responsibility for the entire content of this manuscript and approved its submission.

Conflict of interest: The authors state no conflict of interest.

Data availability statement: The datasets generated and/or analyzed during the current study are available from the corresponding author on reasonable request.

References

[1] Choi SUS, Eastman JA. Enhancing thermal conductivity of fluids with nanoparticles. Argonne National Lab.(ANL), Argonne, IL (United States); 1995.
[2] Galal AM, Akgül A, Idris SA, Formanova S, Ibrahim TK, Hassani MK, et al. The performance evolution of Xue and Yamada-Ota models for local thermal non equilibrium effects on 3D radiative casson trihybrid nanofluid. Sci Rep. 2025;15(1):7325.
[3] Galal AM, Benabdallah F, Bayz DA, Ching DLC, Memon AA, Abbas M, et al. Effect of thermal radiation on Marangoni convective flow of ternary hybrid nanofluid with bioconvection and local thermal non-equilibrium effects. J Radiat Res Appl Sci. 2025;18(2):101378.
[4] Das K. Nanofluid flow over a non-linear permeable stretching sheet with partial slip. J Egypt Math Soc. 2015;23(2):451–6.
[5] Mahmood Z, Alhazmi SE, Alhowaity A, Marzouki R, Al-Ansari N, Khan U. MHD mixed convective stagnation point flow of nanofluid past a permeable stretching sheet with nanoparticles aggregation and thermal stratification. Sci Rep. 2022;12(1):16020.
[6] Khan A, Iqbal Z, Ahammad NA, Sidi MO, Elattar S, Awad S, et al. Bioconvection Maxwell nanofluid flow over a stretching cylinder influenced by chemically reactive activation energy surrounded by a permeable medium. Front Phys. 2023;10:1348.
[7] Poply V. Heat transfer in a MHD nanofluid over a stretching sheet. In: Vega MA, editor. Rijeka: IntechOpen; 2020. p. 11. doi: 10.5772/intechopen.95387.
[8] Ramzan M, Shahmir N, Aljurbua SF, Ghazwani HAS. Numerical study of nanofluid flow over an exponentially stretching sheet with Hall current considering PEST and PEHF temperatures. Waves Random Complex Media. 2022;1–19. doi: 10.1080/17455030.2022.2136779.
[9] Kumar TS. Hybrid nanofluid slip flow and heat transfer over a stretching surface. Partial Differ Equ Appl Math. 2021;4:100070, https://www.sciencedirect.com/science/article/pii/S2666818121000395.
[10] Arif M, Saeed A, Suttiarporn P, Khan W, Kumam P, Watthayu W. Analysis of second grade hybrid nanofluid flow over a stretching flat plate in the presence of activation energy. Sci Rep. 2022;12(1):21565.
[11] Galal AM, Abbas M, Alzahrani AH, Ameen HFM, Khan Y. Local thermal non-equilibrium effects on radiative ternary hybrid nanofluid with thermophoresis and Stefan Blowing impacts: Yamada-Ota and Xue model. J Radiat Res Appl Sci. 2025;18(1):101315.
[12] Abas SA, Ullah H, Islam S, Fiza M. A passive control of magnetohydrodynamic flow of a blood-based Casson hybrid nanofluid over a convectively heated bi-directional stretching surface. ZAMM-J Appl Math Mech Angew Math Mech. 2023;104:e202200576.
[13] Vishalakshi AB, Mahesh R, Mahabaleshwar US, Rao AK, Pérez LM, Laroze D. MHD hybrid nanofluid flow over a stretching/shrinking sheet with skin friction: Effects of radiation and mass transpiration. Magnetochemistry. 2023;9(5):118.
[14] Abas SA, Ullah H, Islam S, Fiza M. Magnetohydrodynamic ternary hybrid nanofluid flow over a stretching surface subject to thermal convective and zero mass flux conditions. Surf Rev Lett. 2024;31(4):1–22.
[15] Abbas N, Rehman KU, Shatanawi W, Malik MY. Numerical study of heat transfer in hybrid nanofluid flow over permeable nonlinear stretching curved surface with thermal slip. Int Commun Heat Mass Transf. 2022;135:106107, https://www.sciencedirect.com/science/article/pii/S0735193322002299.
[16] Lone SA, Alyami MA, Saeed A, Dawar A, Kumam P, Kumam W. MHD micropolar hybrid nanofluid flow over a flat surface subject to mixed convection and thermal radiation. Sci Rep. 2022;12(1):17283.
[17] Kolsi L, Mir A, Muhammad T, Bilal M, Ahmad Z. Numerical simulation of heat and mass transfer through hybrid nanofluid flow consists of polymer/CNT matrix nanocomposites across parallel sheets. Alex Eng J. 2024;108:319–31.
[18] Ahmad Z, Crisci S, Murtaza S, Toraldo G. Numerical insights of fractal–fractional modeling of magnetohydrodynamic Casson hybrid nanofluid with heat transfer enhancement. Math Methods Appl Sci. 2024;47(11):9046–66.
[19] Murtaza S, Becheikh N, Rahman AU, Sambas A, Maatki C, Kolsi L, et al. Thermal performance analysis of a nonlinear couple stress ternary hybrid nanofluid in a channel: A fractal–fractional approach. Nanomaterials. 2024;14(22):1855.

[20] Zangooee MR, Hosseinzadeh K, Ganji DD. Hydrothermal analysis of hybrid nanofluid flow on a vertical plate by considering slip condition. Theor Appl Mech Lett. 2022;12(5):100357.
[21] Abbas M, Bayz DA, Juraev N, Kanwal H, Abbas A, Younis J, et al. Numerical simulation for magnetic dipole in Darcy–Forchheimer flow of diamond-S i C-Co_3O_4/diathermic oil based trihybrid nanofluid with porous medium and arrhenius activation energy. Discov Appl Sci. 2025;7(3):190.
[22] Abbas M, Alzahrani AH, Ameen HFM, Fatima N, Eladeb A, Kanwal H, et al. Thermal radiation effect on Darcy-forchheimer flow of synovial fluid over heated disk: Applications of thermal engineering via two viscosity models. J Radiat Res Appl Sci. 2025;18(2):101369.
[23] Galal AM, Mabrouk A, Ameen HFM, Abbas M, Ching DLC, Sajjad MS, et al. Optimizing flow and heat transfer in industrial processes: The potential of trihybrid nanofluid and thermal-radiation using Hamilton-Crosser and Xue models. J Radiat Res Appl Sci. 2025;18(1):101322.
[24] Dawar A, Shah Z, Tassaddiq A, Kumam P, Islam S, Khan W. A convective flow of Williamson nanofluid through cone and wedge with non-isothermal and non-isosolutal conditions: A revised Buongiorno model. Case Stud Therm Eng. 2021;24:100869.
[25] Paul A, Sarma N, Patgiri B. Mixed convection of shear-thinning hybrid nanofluid flow across a radiative unsteady cone with suction and slip effect. Mater Today Commun. 2023;37:107522.
[26] John AS, Mahanthesh B, Lorenzini G. Study of hybrid nanofluid flow in a stationary cone-disk system with temperature-dependent fluid properties. Appl Math Mech. 2024;45(4):677–94.
[27] Peter F, Sambath P, Dhanasekaran S. Numerical investigation of radiative hybrid nanofluid flows over a plumb cone/plate. Mathematics. 2023;11(20):4331.
[28] Yahaya RI, Mustafa MS, Arifin NM, Pop I, Wahid NS, Ali FM, et al. Mixed convection hybrid nanofluid flow over a stationary permeable vertical cone with thermal radiation and convective boundary condition. ZAMM-J Appl Math Mech Angew Math Mech. 2024;104(4):e202300428.
[29] Dawar A, Islam S, Shah Z, Lone SA. A comparative analysis of the magnetized sodium alginate-based hybrid nanofluid flows through cone, wedge, and plate. ZAMM-J Appl Math Mech Angew Math Mech. 2023;103(1):e202200128.
[30] Iijima S. Helical microtubules of graphitic carbon. Nature. 1991;354(6348):56–8.
[31] Akbar AA, Awan AU, Abbas N. Significance of SWCNTs and MWCNTs on the dynamics of hybrid nanofluid flow over a stretching surface. Waves Random Complex Media. 2022;1–20. doi: 10.1080/17455030.2022.2119299.
[32] Haider SMA, Ali B, Wang Q, Zhao C. Rotating flow and heat transfer of single-wall carbon nanotube and multi-wall carbon nanotube hybrid nanofluid with base fluid water over a stretching sheet. Energies. 2022;15(16):6060.
[33] Kumar TP. Heat transfer of SWCNT-MWCNT based hybrid nanofluid boundary layer flow with modified thermal conductivity model. J Adv Res Fluid Mech Therm Sci. 2022;92(2):13–24.
[34] Nadeem S, Hayat T, Khan AU. Numerical study of 3D rotating hybrid SWCNT–MWCNT flow over a convectively heated stretching surface with heat generation/absorption. Phys Scr. 2019;94(7):75202.
[35] Gupta T, Kumar M, Yaseen M, Rawat SK. Heat transfer of MHD flow of hybrid nanofluid (SWCNT-MWCNT/C3H8O2) over a permeable surface with Cattaneo–Christov model. Numer Heat Transf Part B Fundam. 2023;86:1–16.
[36] Asghar A, Lund LA, Shah Z, Vrinceanu N, Deebani W, Shutaywi M. Effect of thermal radiation on three-dimensional magnetized rotating flow of a hybrid nanofluid. Nanomaterials. 2022;12(9):1566.
[37] El-dawy HA, El-Amin MF, Raizah ZA. Joule heating and viscous dissipation effects on a stretching/shrinking cannel filled by micropolar hybrid nanofluid in presence thermal/solar radiation. J Nanofluids. 2023;12(3):738–44.
[38] Abbas M, Khan N, Hashmi MS, Rezapour S, Inc M. Examination the effects of Stefan blowing on chemical reactive flow of hybrid nanofluid over an infinite disk with Cattaneo-Christove heat flux model. J Taibah Univ Sci. 2025;19(1):2450125.
[39] Khan SA, Khan MI, Khan MR, Alotaibi F, Galal AM. Transportation of Darcy–Forchheimer entropy optimized nonlinear flow toward a stretchable sheet with Ohmic heating and heat generation/absorption. Waves Random Complex Media. 2021;34:1–19.
[40] Ullah H, Abas SA, Fiza M, Jan AU, Akgul A, Abd El-Rahman M, et al. Thermal radiation effects of ternary hybrid nanofluid flow in the activation energy: Numerical computational approach. Results Eng. 2025;25:104062.
[41] Sulochana C, Shivapuji GC. Numerical analysis of hybrid nanofluid flow over a nonlinear stretching sheet with viscous dissipation, Joule heating effects. CFD Lett. 2022;14(10):43–55.
[42] Zhang X-H, Abidi A, Ahmed AE-S, Khan MR, El-Shorbagy MA, Shutaywi M, et al. MHD stagnation point flow of nanofluid over a curved stretching/shrinking surface subject to the influence of Joule heating and convective condition. Case Stud Therm Eng. 2021;26:101184.
[43] Rafique K, Mahmood Z, Adnan, Khan U, Muhammad T, El-Rahman MA, et al. Numerical investigation of entropy generation of Joule heating in non-axisymmetric flow of hybrid nanofluid towards stretching surface. J Comput Des Eng. 2024;11(2):146–60.
[44] Ramzan M, Kumam P, Lone SA, Seangwattana T, Saeed A, Galal AM. A theoretical analysis of the ternary hybrid nanofluid flows over a non-isothermal and non-isosolutal multiple geometries. Heliyon. 2023;9(4):e14875.
[45] Zhou L, Zheng S, Ding S, Xie C, Liu R. Influence of propeller on brash ice loads and pressure fluctuation for a reversing polar ship. Ocean Eng. 2023;280:114624.
[46] Wang L, Xiao K, Xiang G, Cai J, Yang T, Wang J. Study on mixed thermal-visco-hyerelastic hydrodynamic lubrication performance of water-lubricated rubber bearings in deep-sea environment. Tribol Int. 2025;209:110713.
[47] Sun X, Li Z, Zhang L, Tian A, Chai WS, Jing T, et al. Heat transfer augmentation, endothermic pyrolysis and surface coking of hydrocarbon fuel in manifold microchannels at a supercritical pressure. Int Commun Heat Mass Transf. 2025;161:108564.
[48] He J, Hou Q, Yang X, Duan H, Lin L. Isolated slug traveling in a voided line and impacting at an end orifice. Phys Fluids. 2024;36(2):027105.
[49] Cai Y, Wei J, Hou Q, Fan H, Tijsseling AS. A Lagrangian particle model for one-dimensional transient pipe flow with moving boundary. Eng Appl Comput Fluid Mech. 2025;19(1):2452360.
[50] Li N, Morozov IB, Fu L, Deng W. Unified nonlinear elasto-visco-plastic rheology for bituminous rocks at variable pressure and temperature. J Geophys Res Solid Earth. 2025;130(3):e2024JB029295.
[51] Sun W, Liu Y, Xu W, Kan L, Liu H, Zhao L, et al. Study on interaction mechanism between natural convection and forced convection during storage and temperature rise of waxy crude oil tank. Eng Appl Comput Fluid Mech. 2025;19(1):2498354.

[52] Mao Z, Hosoya N, Maeda S. Flexible electrohydrodynamic fluid-driven valveless water pump via immiscible interface. Cyborg Bionic Syst. 2024;5:91.
[53] Wang G, Sun L, Zhang C. The effect of polyvinylpyrrolidone modified nano-polymers on rheological properties of silicon-based shear thickening fluid. Phys Fluids. 2024;36(7):073108.
[54] Wang X, Hu X, Liu Z, Zhu C, Shen R, Quan B, et al. Interpenetrating double-network ANF/MXene-K+ aerogels enable integrated electromagnetic interference shielding, infrared camouflage, and Joule Heating in adaptive multifunctional systems. Nano Res. 2025;7:175.
[55] Zhou Y, Fan S, Zhu Z, Su S, Hou D, Zhang H, et al. Enabling high-sensitivity calorimetric flow sensor using vanadium dioxide phase-change material with predictable hysteretic behavior. IEEE Trans Electron Devices. 2025;72:1360–7.
[56] Zhao Y. Stability of phase boundary between L_{12}-Ni_3Al phases: A phase field study. Intermetallics. 2022;144:107528.
[57] Birkea FMO, Abas SA, Ullah H, Fiza M, Jan AU, Elaissi S, et al. Significance of nanoparticle diameter and inter-particle spacing in the oblique stagnation point flow over a convectively heated cylinder. J Radiat Res Appl Sci. 2025;18(3):101674.
[58] Ajam H, Jafari SS, Freidoonimehr N. Analytical approximation of MHD nano-fluid flow induced by a stretching permeable surface using Buongiorno's model. Ain Shams Eng J. 2018;9(4):525–36.
[59] Tulu A, Ibrahim W. Effects of second-order slip flow and variable viscosity on natural convection flow of (CNTs− Fe_3O_4)/water hybrid nanofluids due to stretching surface. Math Probl Eng. 2021;2021(1):8407194.
[60] Palani G, Lalith Kumar EJ, Kim K-Y. Free convection effects on a vertical cone with variable viscosity and thermal conductivity. J Appl Mech Tech Phys. 2016;57:473–82.
[61] Kumar KA, Reddy JVR, Sugunamma V, Sandeep N. Magnetohydrodynamic Cattaneo-Christov flow past a cone and a wedge with variable heat source/sink. Alex Eng J. 2018;57(1):435–43.